One-, two-, and three-channel Kondo effects for a model Ce^{3+} impurity in a metal

Tae-Suk Kim and D. L. Cox
Department of Physics, Ohio State University, Columbus, Ohio 43210
(Received 24 August 1995; revised manuscript received 26 November 1996)

We present studies of a simple Anderson model Hamiltonian for Ce^{3+} ions in cubic symmetry with three configurations (f^0,f^1,f^2). In different parameter regimes, our model Hamiltonian maps to the one-, two-, and three-channel spin-1/2 Kondo models. Using third-order scaling (perturbative renormalization group) analysis, we study the stability of the non-Fermi-liquid fixed point of the two-channel Kondo model for Ce^{3+} ions in cubic symmetry against the one-channel Kondo interaction. Using the noncrossing approximation (NCA), we also report detailed studies for our simplified model of the competition between the Fermi-liquid fixed point of the one-channel Kondo model and the non-Fermi fixed points of the two- and three-channel Kondo models. We provide the phase diagram in the model parameter space and study the thermodynamics and the transport properties of our simplified model Hamiltonian. Thermodynamics and transport coefficients show distinct behaviors for different numbers of channels. We confirm in detail that the NCA is a valid numerical method for the overcompensated multichannel $S_I=1/2$ Anderson models. Our model study might be relevant to the non-Fermi-liquid alloy $Ce_{1-x}La_xCu_{2.2}Si_2$. [S0163-1829(97)02313-8]

I. INTRODUCTION

The Kondo effect[1] has been of great interest in condensed matter physics since its observation. The proposed model Hamiltonian, a magnetic $S_I=1/2$ local moment interacting with the conduction electron gas, looked very simple but was nontrivial due to the many-body nature of the problem. Ever since, many generalized models have been studied to extend our understanding and to relate to real materials. The simplest $S_I=1/2$ orbitally nondegenerate Anderson model[2] and *s-d* exchange model are now well understood for a single-impurity case using several techniques. The numerical renormalization group (NRG) (Ref. 3) method was able to provide complete information about the crossover from the high-temperature fixed point to the low-temperature Fermi-liquid fixed point for these models. Subsequently, the exact diagonalization of these models was realized by the Bethe ansatz (BA),[4] which also gives an exact solution for the thermodynamics of these models. However, it has not proved possible to compute dynamical properties with the BA. Through the noncrossing approximation (NCA),[5] dynamics as well as thermodynamics[6] have been extensively studied for the infinite on-site Coulomb interaction models. The quantum Monte Carlo method (QMC) (Ref. 7) has also been applied to study statics and dynamics for the simple $S_I=1/2$ models. Recently conformal field theory (CFT) (Refs. 8 and 9) has been used to study all properties asymptotically close to the low-temperature fixed points.

However, we are still far from a complete understanding for realistic models which, for example, include the strong spin-orbit coupling, crystalline electric field (CEF) effects, and multiple (more than two) configurations. In this paper, we study a realistic extension of the conventional simple approach to the Kondo effect for Ce^{3+} ions, including strong spin-orbit coupling, crystalline electric field effects, and multiple configurations.

In generalizing the Kondo model, Nozières and Blandin[10] introduced the multichannel Kondo model. This model consists of M bands of $S_c=1/2$ conduction electrons coupled to a spin S_I impurity through an antiferromagnetic Heisenberg exchange interaction. There are three regimes of the model: (i) *Compensated*. Here $M=2S_I$ so that there is precisely enough conduction spin to quench the impurity. In this case, the impurity moment vanishes at low temperatures as in the conventional Kondo effect ($M=1=2S_I$ for $S_I=1/2$). It is widely believed that this model describes the Kondo effect for Mn ions in metallic hosts, since the Mn has a half-filled *d* shell with a ''pure spin'' ground state and, hence, negligible crystal field and spin-orbit effects (here $M=5$ and $S_I=5/2$). (ii) *Undercompensated*. Here $M<2S_I$ so that there is not enough conduction spin to quench the impurity, and as Nozières and Blandin[10] argued, this will lead to a ground-state impurity moment of $S_I-M/2$ with residual ferromagnetic coupling to the conduction electrons. (iii) *Overcompensated*. In this case, $M>2S_I$, and so there is more conduction spin than needed to quench the impurity. Nozières and Blandin[10] argued that this will give rise to a nontrivial fixed point with a non-Fermi-liquid excitation spectrum and critical behavior in thermodynamic and dynamic quantities.

The possibility of the experimental realization of the most interesting overcompensated fixed point has been controversial since its inception, when, in the context of *d* ions, Nozières and Blandin[10] argued that it would likely never be observed. On the theoretical side, the multichannel Kondo model is well understood[8,11–13] irrespective of the experimental situation. For example, the spin susceptibility $\chi(T)$ and specific heat coefficient $C(T)/T$ for the two-channel $S_I=1/2$ magnetic Kondo model are proportional to $\ln(T_K/T)$ at low temperatures,[8,9,11–13] where T_K is the Kondo energy scale separating the high-temperature perturbative regime from the low-temperature nonperturbative regime. The dynamic susceptibility shows marginal Fermi-liquid behavior.[14] The resistivity increases logarithmically up to T_K as the temperature is lowered and saturates to a constant below T_K, with $\rho(T)\approx\rho(0)[1-a\sqrt{T/T_K}]$ as $T\to 0$[8]. On the

other hand, the one-channel $S_I=1/2$ Kondo model leads to the Fermi-liquid ground state. In that case, the magnetic susceptibility $\chi(T)$ and specific heat coefficient $C(T)/T$ saturate to constants of order $1/T_K$.[3,4] The resistivity increases logarithmically as T is lowered to T_K and saturates to a constant below T_K with $\rho(T)\approx\rho(0)[1-a(T/T_K)^2]$ for $T\rightarrow 0$.[15]

In this paper we study a model Hamiltonian for Ce^{3+} ions in cubic metals with three configurations (f^0, f^1, f^2). The nominal ground configuration f^1 can fluctuate to f^0 and f^2 configurations by hybridizing with the conduction electrons. A one-channel Anderson hybridization interaction is present between f^0 and f^1 configurations. A two-channel Anderson hybridization interaction is present between f^1 and f^2 configurations. We report detailed studies of our simplified Hamiltonian using the NCA. This simple model is quite intriguing in that we can study the competition between the two different Kondo effects, that is, the Fermi-liquid fixed point of the $M=1$, $S_I=1/2$ model and the non-Fermi-liquid fixed points of the $M=2,3$, $S_I=1/2$ models. The distinct ground-state physics for different numbers of channels is classified using the zero-temperature analysis of NCA integral equations and third-order scaling (perturbative renormalization group) theory. We calculate the thermodynamics and dynamics of this simple model and find that all the calculated physical quantities show a behavior corresponding to different channel numbers in the appropriate parameter regimes. The static magnetic susceptibility displays a scaling behavior in excellent agreement with the exact Bethe ansatz results in the two- and three-channel cases. The NCA calculation of the entropy and specific heat is also compared with the Bethe ansatz results. The resistivity shows the correct temperature dependence near zero temperature, agreeing with the conformal field theory results in the two- and three-channel cases. The sign and magnitude of the thermopower are dependent sensitively on the relevant channel numbers. The peak position in the dynamic magnetic susceptibility is almost linear in temperature in the overscreened cases. A short paper which presents some of these results has appeared elsewhere.[16]

Our study is motivated in part by a recent discovery of the non-Fermi-liquid system $Ce_xLa_{1-x}Cu_{2.2}Si_2$ ($x=0.1$).[17] Here, we briefly summarize the experimental findings of this alloy system. The logarithmic divergence in both the magnetic susceptibility $\chi(T)$ and the specific heat linear coefficient $\gamma(T)$ has been observed for $Ce_xLa_{1-x}Cu_{2.2}Si_2$ ($x=0.1$). The two-channel $S_I=1/2$ magnetic Kondo physics[8,9,11–13] provides a theoretical framework to explain the thermodynamics of this system at low temperatures. $\gamma(T)$ initially increases in the presence of the magnetic field, which qualitatively agrees with the two-channel Kondo effect coming from the lifting of residual entropy.[13] In the one-channel Kondo effect, the Sommerfeld coefficient decreases in the magnetic field due to the destruction of the Kondo effect. The Wilson ratio is estimated to be $R\approx 2.7$ from the slopes of two curves [$\chi(T)$ and $\gamma(T)$], which compares well with the theoretical value 8/3 for the two-channel magnetic $S_I=1/2$ Kondo model.[9] The good agreement between the theoretical and the experimental Wilson ratios supports our crystalline electric field energy scheme described below. This system is pseudocubic (i.e., the crystal field scheme on the Ce^{3+} site appears cubic). The best superconducting system with excess Cu shows almost isotropic magnetic susceptibility.[18] That the pseudocubic Γ_7 magnetic doublet in f^1 lies lowest is inferred from neutron scattering experiments.[19] The thermopower for $CeCu_2Si_2$ changes sign near 70 K and stays negative below with a large extremum (-20 to -30μV/K),[18] suggesting the presence of strong hole resonance scattering. As we will show below, these thermopower results also support our interpretation of the two-channel magnetic Kondo physics. Though other experiments (e.g., specific heat and magnetic susceptibility) support the interpretation of them in terms of the two-channel Kondo effect, the linear temperature dependence in the resistivity remains as a puzzle. The $\sqrt{T}$ behavior in the resistivity is predicted from a conformal field theory treatment of two-channel Kondo models.[8,9] In Fig. 1, we present our numerical calculation of the resistivity and experimental results measured in the alloy system $Ce_xLa_{1-x}Cu_{2.2}Si_2$ ($x=0.1$).[17] It can be seen that the data curve downwards at lower temperature, which may indicate a crossover to a new fixed point. From all these experimental findings, we believe that the alloy system $Ce_xLa_{1-x}Cu_{2.2}Si_2$ ($x=0.1$) is a strong candidate for a two-channel $S_I=1/2$ magnetic Kondo system. However, we do note that the experimental thermopower of the dilute system is positive,[20] which may mitigate the relevance of the two-channel model to this alloy.

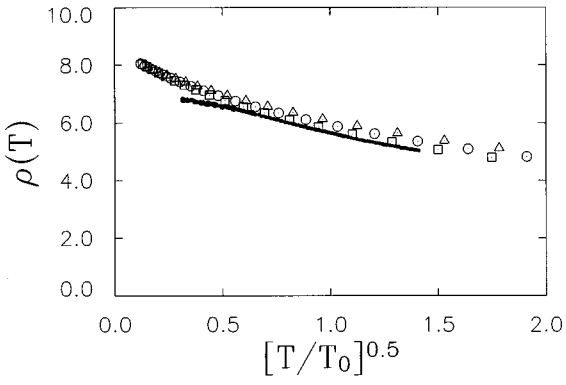

FIG. 1. Comparison of experimental resistivity with our numerical calculation. Our numerical calculation shows a $T^{1/2}$ behavior at low temperatures. The experimental resistivity (points with $T_0=10$ K) from Ref. 17 is compared with our numerical results. The three different symbols refer to three sets of model parameters (□ for model set 1, ○ for model set 2, △ for model set 3). The low-temperature deviation suggests a possible crossover to a new fixed point.

In addition, the two-channel, $S_I=1/2$ Kondo effect may be realized in other materials, notably through the two-channel quadrupolar Kondo effect[21] in some U alloys and the two-level system Kondo effect[22] in metallic point contacts. Candidate U alloy systems include $U_{0.2}Y_{0.8}Pd_3$,[23] $U_xTh_{1-x}Ru_2Si_2$,[24] $UCu_{3.5}Pd_{1.5}$,[25] $U_{0.1}Th_{0.9}Ni_2Al_3$,[26] $U_{0.1}Pr_{0.9}Ni_2Al_3$,[26] $U_xSc_{1-x}Pd_3$,[27] $U_{0.9}Th_{0.1}Be_{13}$,[28] and $U_xTh_{1-x}Pd_2Al_3$.[29] All the above systems show a logarithmic divergence at low temperature in the linear specific heat coefficient and a different temperature dependence to the static magnetic susceptibility, compatible with a quadrupolar Kondo effect. $U_xTh_{1-x}Ru_2Si_2$ (Ref. 24) (together, possibly, with $U_{0.1}Th_{0.9}Ni_2Al_3$, $U_{0.1}Pr_{0.9}Ni_2Al_3$, and

$U_xTh_{1-x}Pd_2Al_3$) is an exception, showing a logarithmically divergent magnetic susceptibility. The two-channel quadrupolar Kondo physics has been invoked to explain the non-Fermi-liquid behavior in the thermodynamic and transport properties of $U_xY_{1-x}Pd_3$ for $x=0.2$ (Ref. 23) and other U alloy systems. Recently, the resistivity in a metallic constriction was observed to obey $\sqrt{T}$ behavior and was interpreted as due to two-channel Kondo scattering from atomic two-level tunneling systems.[30,31]

Our paper is organized as follows. In Sec. II, we introduce our simple model Hamiltonian and analyze this model using third-order scaling (perturbative renormalization group) theory. We briefly introduce the NCA in Sec. III. A zero-temperature analysis of NCA integral equations follows in Sec. IV. In Sec. V, we present detailed numerical analysis of our simple model Hamiltonian using the NCA. We conclude and discuss possible research directions in Sec. VI.

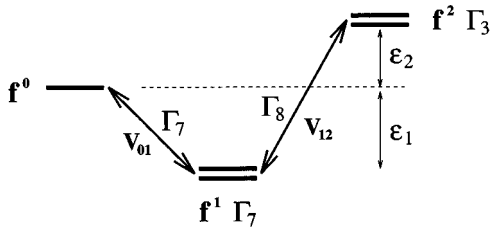

FIG. 2. Crystal electric field energy level scheme for f^0, f^1, f^2 configurations. The one-channel and two-channel Anderson model Hamiltonians are developed from these CEF energy states. The one-channel Kondo model derives from the f^0 singlet and the magnetic $f^1\Gamma_7$ doublet which mix through hybridization with the Γ_7 conduction electrons. The two-channel Kondo model derives from the magnetic $f^1\Gamma_7$ doublet and the nonmagnetic $f^2\Gamma_3$ doublet which mix through hybridization with the Γ_8 conduction electrons.

II. MODEL HAMILTONIAN

The single-impurity one-channel Anderson model[2] has been very successful[6] in describing Kondo systems (meaning magnetic transition metal elements embedded in normal metals and dilute rare earth or actinide alloys). The thermodynamics is rather well explained by the single-impurity properties for even highly concentrated Ce alloys.[6,32] Coherence effects, arising from the lattice of Anderson or Kondo ions at low temperatures, do not play an important role in thermodynamics. Transport properties also are well explained by the single-impurity model except for the low-temperature regime where coherent Bloch state formation leads to a vanishing resistivity at zero temperature (the residual resistivity is larger than the room-temperature value in the dilute impurity limit). This one-channel Anderson model can explain the complete screening of the magnetic moment at the local moment sites, leading to the local Fermi-liquid ground state discussed in the Introduction.

Our primary interest in this paper is to examine, in our simplified model, the conditions under which a Ce^{3+} ion in a metal can undergo a two- or three-channel Kondo effect. In general, the stability of the two- or three-channel ground state can be tricky to realize since realistic perturbations can destabilize the fixed point. For example, even for a single two-channel orbital Kondo impurity (quadrupolar or two-level system) the channel symmetry is guaranteed by time-reversal symmetry, but the ground-state degeneracy may be lifted by the Jahn-Teller effect.[33] In general, the orbital Kondo model has exchange anisotropy. It has been shown that exchange anisotropy is irrelevant for two-channel $S_I=1/2$ Kondo models.[34] As shown in another publication,[35] the two-channel magnetic Kondo fixed point for Ce^{3+} is unstable to the perturbation of channel asymmetry due to the orbital nature of the channel degrees of freedom;[10] one such term arises naturally in the Schrieffer-Wolff transformation integrating out virtual f^1-f^2 fluctuations.[35,36] However, the same Schrieffer-Wolff transformation generates the channel-mixing Kondo interaction that restores the stability of the two-channel fixed point.[35] We direct the reader to this latter reference for more details on this surprising result.

A common assumption in modeling Ce^{3+} impurities is to take the simplifying limit of infinite on-site Coulomb interactions, which removes the f^2 configuration from consideration[6], and, as a result, has no chance to get the two-channel Kondo effect, which we shall explain below. When we relax the assumption about infinite on-site Coulomb interactions and we include detailed atomic energy structure, we can develop a variety of model Hamiltonians.[35]

In the simplest model, which we study in this paper, we assume that the magnetic $f^1J=5/2\Gamma_7$ CEF doublet lies lowest in the f^1 configuration, and we keep two excited states—a singlet from the f^0 configuration and the nonmagnetic $f^2\Gamma_3$ CEF doublet. We find the one-channel Anderson model in mixing between f^0 and f^1 configurations and the two-channel Anderson model in mixing between f^1 and f^2 configurations.[37] Other interesting Kondo interactions[35] arise when the excited triplets in the f^2 configuration are included.

According to group theoretic analysis, the hybridization is mediated only by the cubic Γ_8 conduction electrons between f^1 and f^2 ($\Gamma_3\otimes\Gamma_7=\Gamma_8$) and by Γ_7 between f^0 and f^1 for the mixing potential allowed in the cubic crystal. CEF states are schematically drawn in Fig. 2 for this simple model. To see the essential physics, we restrict our attention to the simple case of isotropic hybridization and a free conduction band with Lorentzian-Gaussian density of states (DOS). In this simple case, two components of the conduction partial waves $l_c=3$, $j_c=5/2,7/2$, can mix with the atomic orbitals. The dominant hybridization is expected to be in the $l_c=3$ channel due to the primary f character of the Ce^{3+} states. In this paper we will consider only the $l_c=3$, $j_c=5/2$ partial waves of the conduction band for our model study. Under the action of the crystal field, these partial waves will be split into a Γ_7 doublet and Γ_8 quartet. The former couples the f^0 and f^1 configurations exclusively, and comes in effectively as a single $S=1/2$ conduction band in our model. The quartet couples the f^1 and f^2 configurations together and may be viewed as two $S=1/2$ bands, given that the irreducible representation may be written as a tensor product of ''spin'' (Γ_7) and ''orbital'' (Γ_3) states through the identity $\Gamma_8=\Gamma_7\otimes\Gamma_3$. The effects of relaxing the assumption of $j_c=5/2$ partial waves is studied extensively in Ref. 35.

With the above assumptions, our model Hamiltonian is

$$H=H_{\rm cb}+H_{\rm at}+H_1, \tag{1}$$

$$H_{\rm cb}=\sum_{\epsilon\alpha}\ \epsilon c^{\dagger}_{\epsilon\Gamma_7\alpha}c_{\epsilon\Gamma_7\alpha}+\sum_{\epsilon n\alpha}\ \epsilon c^{\dagger}_{\epsilon\Gamma_8 n\alpha}c_{\epsilon\Gamma_8 n\alpha}, \tag{2}$$

$$H_{\rm at}=\epsilon_0|f^0\rangle\langle f^0|+\epsilon_1\sum_{\alpha}\ |f^1\Gamma_7\alpha\rangle\langle f^1\Gamma_7\alpha|$$

$$+\epsilon_2\sum_{n}\ |f^2\Gamma_3 n\rangle\langle f^2\Gamma_3 n|, \tag{3}$$

$$H_1=V_{01}\sum_{\epsilon\alpha}\ c^{\dagger}_{\epsilon\Gamma_7\alpha}|f^0\rangle\langle f^1\Gamma_7\alpha|+\text{H.c.}$$

$$+V_{12}\sum_{\epsilon n\alpha}\ (-1)^{\alpha+1/2}c^{\dagger}_{\epsilon\Gamma_8 n\alpha}|f^1\Gamma_7\overline{\alpha}\rangle\langle f^2\Gamma_3 n|+\text{H.c.}, \tag{4}$$

where $c_{\epsilon\Gamma_7\alpha}$ ($c^{\dagger}_{\epsilon\Gamma_7\alpha}$) and $c_{\epsilon\Gamma_8 n\alpha}$ ($c^{\dagger}_{\epsilon\Gamma_8 n\alpha}$) are the annihilation (creation) operators for conduction electrons of Γ_7 and Γ_8, respectively. The label $\alpha=\uparrow,\downarrow$ denotes the time-reversal pair of states in the Γ_7 irreducible representation, and $n=\pm$ is the quadrupolar index for the Γ_3 irreducible representation which acts here as the channel index. The conduction electrons are assumed to be described by an uncorrelated Lorentzian-Gaussian density of states with bandwidth $D=3$ eV. Here $\epsilon_{0,1,2}$ are the configuration energies for the empty ($\epsilon_0=0$), singly occupied, and doubly occupied configurations, respectively. We have lumped all Clebsch-Gordon coefficients into the hybridization constants V_{01} and V_{12}, except for the phase dependence on the cubic degeneracy indices. The phase dependence on the Kramers doublet index arises from proper consideration of time-reversal symmetry. We will consider these two hybridization constants to be independent of each other in this study in order to probe the competition between the one-channel and two-channel Kondo physics.

We note that in the language of the single-channel Anderson model, ϵ_1 corresponds to ϵ_f and ϵ_2 corresponds to $2\epsilon_f+U_{ff}$. For real Ce^{3+} ions, $\epsilon_f\approx-2$ eV and $U_{ff}\approx5$–6 eV,[38] and so one would expect $\epsilon_2\approx1$–2 eV. However, in this simple model we shall consider situations in which ϵ_2 is zero or negative. This unrealistic choice is a limitation of the simplicity of our model, in which we try to represent the *nine* Γ_3 doublets of the f^2 configuration by a single state. Indeed, it may be seen that a generalized NCA including all nine of these doublets leads to a correctly enhanced Kondo scale for the two-channel coupling which sums the effective exchange integrals of all the doublets,[39] which we discuss later in this section and in Appendix A.

When the real charge fluctuations are removed from the model system in the Kondo limit, we have to construct tensor operators representing each CEF state for the f^1 configuration and couple these to tensor operators from the partial wave and CEF projected conduction electron CEF states. In this paper, the relevant tensor operators are for $\Gamma_{7,8}$ CEF states. We can show using the standard means of character table decomposition of tensor products of irreducible representations[40] that

$$\Gamma_7\otimes\Gamma_7=\Gamma_1\oplus\Gamma_4, \tag{5}$$

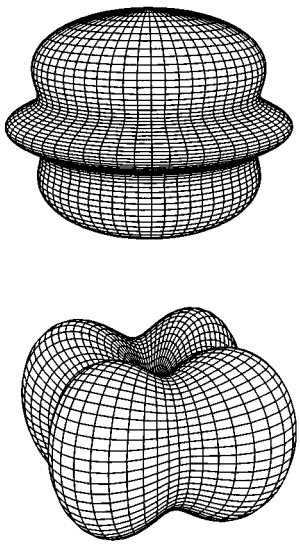

FIG. 3. Schematic diagrams of two channel degrees of freedom. The upper figure is for Γ_8+ and the lower figure for Γ_8- of $J=5/2$ conduction electron partial waves. Each orbital shape measures a channel label.

$$\Gamma_8\otimes\Gamma_8=\Gamma_1\oplus\Gamma_2\oplus\Gamma_3\oplus2\Gamma_4\oplus2\Gamma_5. \tag{6}$$

In the direct product, the first CEF states are written as ket and the second as bra. The Γ_7 tensor operator product (2×2 tensor) decomposes into the direct sum of a charge operator (Γ_1) and a trio of spin operators (Γ_4). Indeed, the Schrieffer-Wolff transformation leads to two interaction terms: the spin exchange interaction and the pure potential scattering term. The relevant terms of Γ_8 tensor operators are the $2\Gamma_4$ irreps in our model; these are spin operators which may be formed from the $j_c=5/2,\Gamma_8$ partial waves. In the conduction electron Γ_8 tensor space, one of the two Γ_4's gives rise to the ordinary $S_c=1/2$ spin operators with two degenerate orbital channels and the other to one channel of $S_c=3/2$ spin operators.[35]

We note that the other operators in the $\Gamma_8\otimes\Gamma_8$ tensor space are not relevant here as they cannot couple to the impurity tensors. One set of the Γ_5 irrep tensors is (dominantly) quadrupolar tensors of xz,yz,xy character. The $\Gamma_2\oplus\Gamma_3$ irrep tensors are, respectively, a predominantly magnetic octupole operator ($\sim J_xJ_yJ_z$) and an irreducible representation pair of predominantly quadrupolar $[\sim J_x^2-J_y^2,3J_z^2-J(J+1)]$ operators. They are responsible for the two-channel quadrupolar Kondo coupling to a Γ_3 ground doublet for U^{4+} and Pr^{3+} ions in cubic symmetry.[21,37]

Hence, there are three distinct channel labels for conduction electron partial wave states about the Ce impurity in this simple model. One channel is just the Γ_7 doublet. The other two are the $\Gamma_3\pm$ ''orbital'' states of the Γ_8 quartet. Each $\Gamma_3\pm$ orbital has a Γ_7 ''spin'' doublet (recall $\Gamma_8=\Gamma_7\otimes\Gamma_3$.) As shown in Fig. 3 for $J=5/2$ conduction partial waves, the $+$ orbital is ''stretched'' along the quantized axis (one of the three principal cubic axes, taken to be $\hat{z}$ here for definiteness.) The ''$-$'' orbital is ''squashed'' in the xy plane. We note that the simplest example of a Γ_8 partial wave quartet

is, for zero spin-orbit coupling, d-wave states with $+\rightarrow 3z^2-r^2$ and $-\rightarrow x^2-y^2$. The ''spin'' index is then real spin of the electrons.

In the Kondo limit with a stable f^1 configuration, we may remove the f^0-f^1, f^1-f^2 charge fluctuations from the Hamiltonian of Eq. (4) using the Schrieffer-Wolff transformation[41] to find the effective Hamiltonian.

$$\widetilde{H}_1 = J_1 \vec{S}_{c\Gamma_7}(0)\cdot\vec{S}_{\Gamma_7} + J_2 \sum_{n=\pm} \vec{S}_{c\Gamma_8 n}(0)\cdot\vec{S}_{\Gamma_7}, \tag{7}$$

$$J_1 = \frac{2|V_{01}|^2}{-\epsilon_1}, \quad J_2 = \frac{2|V_{12}|^2}{\epsilon_2-\epsilon_1}, \tag{8}$$

$$\vec{S}_{\Gamma_7} = \frac{1}{2}\sum_{\alpha\beta} |f^1;\Gamma_7\alpha\rangle\vec{\sigma}_{\alpha\beta}\langle f^1;\Gamma_7\beta|. \tag{9}$$

$\vec{S}_{\Gamma_7}$ is the f^1 pseudospin. $\vec{S}_{c\Gamma_7}(0)$ and $\vec{S}_{c\Gamma_8\pm}(0)$ are the conduction electron pseudospin densities at the impurity site of symmetry Γ_7 and Γ_8, respectively. When the f^1 configuration is stable, its pseudospin is coupled to the conduction band in a one-channel via f^0 configuration and in a two-channel via f^2 configuration. Both couplings are antiferromagnetic. The unique feature of our Hamiltonian is that it can generate one-, two-, and three-channel ground states depending on the model parameters. The competition between the Fermi-liquid fixed point and the non-Fermi-liquid fixed points can thus be investigated using this model Hamiltonian.

We first analyze our simple model Hamiltonian using third-order scaling arguments, i.e., the perturbative renormalization group (RG).[10,42] At a given temperature T, only the thermally excited conduction electrons within an effective bandwidth of order T about the Fermi level play an important role in determining physical properties. Thus we can integrate out the band edge states (virtually excited states) to find the effective Hamiltonian. Though the following analysis is restricted to energies $|\omega|, T \ll D$ and the perturbative regime (weak-coupling limit), we can obtain qualitatively correct results from this study. For quantitative results, a full numerical renormalization group (NRG) study is required.

It can be deduced from the scaling theory that the low-temperature and low-energy physics is dominated by the one-channel or two-channel Kondo effect depending on its relative magnitude of the antiferromagnetic couplings. To see this, we introduce an exchange coupling matrix in the channel space which is convenient for the derivation of the scaling equations. We can thus rewrite the one-channel and two-channel Kondo models in the form[35]

$$\widetilde{H}_1 = \mathbf{J}\otimes\vec{S}_c(0)\cdot\vec{S}_I, \tag{10}$$

$$\mathbf{J} = \begin{pmatrix} J_1 & 0 & 0 \\ 0 & J_2 & 0 \\ 0 & 0 & J_2 \end{pmatrix}. \tag{11}$$

Here $\vec{S}_c$ and $\vec{S}_I$ are $S=1/2$ operators. The scaling equations of our simple model Hamiltonian up to the third-order diagrams of Fig. 4 are

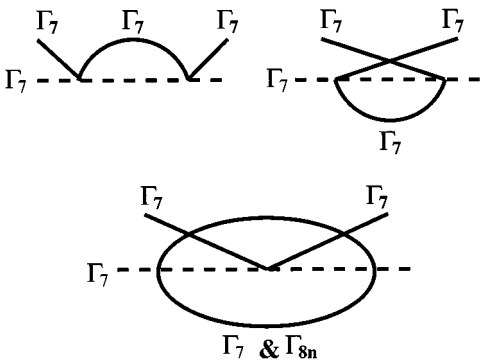

FIG. 4. Scaling diagrams of one-channel and two-channel Anderson model up to third order. Dashed lines are for the Ce^{3+} impurity Γ_7 pseudospins and the solid lines are for the Γ_7 or Γ_{8n} conduction electrons. The diagrams labeled as above lead to the scaling equation for the one-channel exchange coupling J_1. To obtain the scaling equations for the two-channel exchange coupling J_2, the labels Γ_7 for the external conduction electrons (solid lines) should be replaced by Γ_{8n}.

$$\frac{\partial \mathbf{g}}{\partial x} = \mathbf{g}^2 - \frac{1}{2}\mathbf{g}\mathrm{Tr}[\mathbf{g}^2], \tag{12}$$

$$\mathbf{g} = N(0)\mathbf{J}. \tag{13}$$

The scaling equations in components are

$$\frac{\partial g_1}{\partial x} = g_1^2 - \frac{1}{2}g_1[g_1^2+2g_2^2], \quad g_1 = N(0)J_1 > 0, \tag{14}$$

$$\frac{\partial g_2}{\partial x} = g_2^2 - \frac{1}{2}g_2[g_1^2+2g_2^2], \quad g_2 = N(0)J_2 > 0. \tag{15}$$

Here $x=\ln(D/T)$. We can identify three fixed points related to one-, two-, and three-channel Kondo physics. The one-channel, strong-coupling fixed point $(g_1^*, g_2^*)=(\infty,0)$ is stable, leading to the Fermi-liquid ground state.[42] The three-channel fixed point (2/3,2/3) is stable along the line $g_1=g_2$ in the g_1-g_2 plane, but unstable for any small perturbation from $g_1=g_2$. Finally, the two-channel fixed point (0,1) is stable, leading to the logarithmically divergent thermodynamic properties at zero temperature. From the scaling analysis, we can infer the ground-state physics: one channel for $J_1>J_2$, two channel for $J_1<J_2$, and three channel for $J_1=J_2$. As will be shown in Sec. IV, a zero-temperature analysis of the NCA equations leads to the same conclusion.

We now discuss the neglected Γ_3 irreps in the f^2 configuration.[35] The nine Γ_3 CEF states all contribute to the enhancement of the two-channel exchange coupling between $f^1\Gamma_7$ spin and the Γ_8 conduction electron spins:

$$H_1 = \sum_{\epsilon}\sum_{in\alpha} (-1)^{\alpha+1/2} V_{12}^i c^\dagger_{\epsilon\Gamma_8 n\alpha} |f^1\Gamma_7\overline{\alpha}\rangle\langle f^2\Gamma_3^i n| + \mathrm{H.c.} \tag{16}$$

The NCA can treat this problem with the extension that now the $f^2\Gamma_3$ Green's function becomes a 9×9 matrix. See Appendix A for more details. The Schrieffer-Wolff transformation leads to

$$\widetilde{H}_1 = J \sum_{n=\pm} \vec{S}_{c\Gamma_8 n}(0) \cdot \vec{S}_{\Gamma_7}, \tag{17}$$

$$J = \sum_{i=1}^{11} \frac{2|V_{12}^i|^2}{\epsilon_2^i - \epsilon_1}. \tag{18}$$

Here ϵ_2^i is the energy level for the ith $f^2\Gamma_3$ state. Hence multiple Γ_3 states in the f^2 configuration lead to an enhancement of the two-channel exchange coupling.

Particle-hole asymmetry in the conduction band density of states (DOS) is also important in determining the ground-state weights of the one-channel (f^0-f^1) and the two-channel (f^1-f^2) contributions. In our scaling approach, the particle-hole asymmetry is completely neglected, though it is in principle possible to include. However, the NCA can take into account this particle-hole asymmetry. The occupied conduction electron states (holes) contribute to the f^0 self-energy (see Sec. III), while the unoccupied states (particles) contribute to the f^2 self-energy. Hence increased weight on the particle side can enhance the effective hybridization strength between f^1 and f^2 configurations. Alternatively, a conduction band DOS with dominant particle weight will lead to the enhancement of the two-channel exchange coupling.

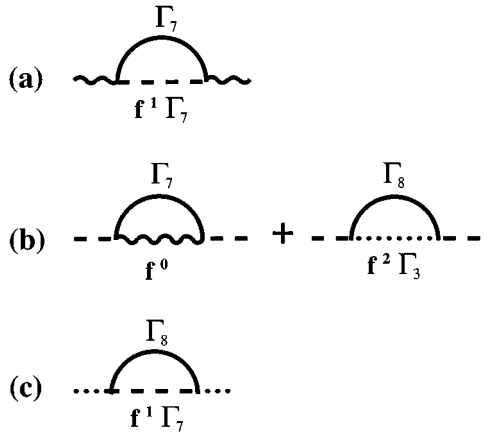

FIG. 5. Leading skeleton self-energy diagrams from the NCA. Since two different symmetry conduction electrons are involved in the hybridizations of f^0-f^1 and f^1-f^2, our NCA self-energy diagrams become simplified. The diagram (a) is the self-energy for the f^0 atomic state (wiggly line). Diagrams (b) are for the $f^1\Gamma_7$ atomic state (dashed line). Diagram (c) is for the $f^2\Gamma_3$ atomic state (dotted line). The solid line is the conduction electron propagator: The first two are for the Γ_7 and the second two are for the Γ_8 conduction electrons.

III. NONCROSSING APPROXIMATION

We now apply the noncrossing approximation (NCA) (Ref. 5) to study our simple model system. This model is highly simplified as compared with the full model[35] which can have stable one-, two-, and three-channel fixed points together with an infinite number of unstable fixed points. However, we can use this simple model Hamiltonian to study the properties of the competing $M=1,2,3$ fixed points of the full Hamiltonian.

In the NCA, our starting basis is the conduction band plus the atomic Hamiltonian projected to the atomic electron Fock space with the hybridization between the conduction band and the atomic orbital treated as a perturbation. The strength of this approach is that the strong on-site Coulomb interaction for atomic electrons is treated accurately at the outset. Pseudoparticle Green's functions are introduced for each atomic electron occupation state. The price we pay is that we cannot apply conventional Feynmann diagram techniques to this strongly correlated problem. Thus special Green's function techniques have been developed by many investigators.[5,6,43–46] This approach may be justified as a self-consistent expansion in the inverse of the ground-state degeneracy, $1/N$, which reorders the diagrams by treating NV^2 as $\mathcal{O}(1)$. In the NCA, pseudoparticle self-energy diagrams include only the leading-order skeleton (noncrossing) diagrams and they are solved self-consistently. For the one-channel models, this theory includes all the diagrams up to $\mathcal{O}(1/N)$ order together with an infinite-order subset of higher-order diagrams. Vertex corrections, of order $(1/N^2)$, are not included. This approach has been shown to be a conserving approximation.[44] For the overscreened multichannel Anderson models, it has been shown[14] that the $1/N$ approach becomes exact in the limit $M,N\to\infty$ with fixed M/N ratio (M is the number of channels).

When we study the most general three-configuration model, the same symmetry conduction electron can be involved in the two mixing processes, e.g., f^0-f^1 and f^1-f^2 for Ce^{3+} atoms. Generally, a specific vertex correction is required to get the right Kondo energy scales in this case. Recently, such vertex corrections were included in the study of the finite-U spin-1/2 Anderson model.[47] A nice feature of our model Hamiltonian is that this leading vertex correction vanishes, since two different symmetry conduction electrons are involved in the hybridizations f^0-f^1 (Γ_7) and f^1-f^2 (Γ_8). This feature greatly simplifies the numerical work and formalism.

From the leading-order skeleton diagrams of Fig. 5, we find the self-consistent NCA integral equations

$$\Sigma_0(z) = \frac{\Gamma_{01}}{\pi} \sum_\alpha \int d\epsilon \widetilde{N}(\epsilon) f(\epsilon) G_1(z+\epsilon), \tag{19}$$

$$\Sigma_1(z) = \frac{\Gamma_{01}}{\pi} \int d\epsilon \widetilde{N}(\epsilon) f(-\epsilon) G_0(z-\epsilon) + \frac{\Gamma_{12}}{\pi} \sum_n \int d\epsilon \widetilde{N}(\epsilon) f(\epsilon) G_2(z+\epsilon), \tag{20}$$

$$\Sigma_2(z) = \frac{\Gamma_{12}}{\pi} \sum_\alpha \int d\epsilon \widetilde{N}(\epsilon) f(-\epsilon) G_1(z-\epsilon), \tag{21}$$

$$G_N(z) = \frac{1}{z - \epsilon_N - \Sigma_N(z)}, \quad \Gamma_{ij} \equiv \pi N(0) |V_{ij}|^2. \tag{22}$$

Here $\widetilde{N}(\epsilon)$ is the conduction band DOS at the Fermi level normalized so that $\widetilde{N}(0)=1$. Here $\Sigma_{0,1,2}(z)$ and $G_{0,1,2}(z)$ are the self-energy equations and Green's functions for f^0, $f^1\Gamma_7$, and $f^2\Gamma_3$ atomic states, respectively. $f(\epsilon)$ is the Fermi-Dirac distribution function. $\Gamma_{ij} = \pi N(0) V_{ij}^2$ is the hybridization strength characterizing the width of the renormal-

ized atomic electron spectral function peak. One of the strong points of the NCA approach is that we can easily study any form of the conduction band DOS, as opposed to, e.g., Bethe ansatz or conformal field theory methods. For simplicity here, however, we use structureless Lorentzian, Gaussian DOS to get at the low-energy many-body physics. We will solve the above coupled integral equations numerically and analytically (in the low-temperature limit) to study the thermodynamics and dynamics of the model Hamiltonian.

Note that pseudoparticle Green's functions are not directly measurable. All the physically measurable quantities are given by suitable convolutions of the pseudoparticle Green's functions. Now it is convenient to introduce the spectral function $[A_N(\omega)]$ for each pseudoparticle Green's function and its corresponding ''negative-frequency'' spectral function $[a_N(\omega)]$. These are defined by

$$A_N(\omega) \equiv -\frac{1}{\pi}\mathrm{Im}\frac{1}{\omega-\epsilon_N-\Sigma_N(\omega)}, \tag{23}$$

$$a_N(\omega) \equiv e^{-\beta\omega}A_N(\omega). \tag{24}$$

The negative-frequency spectra play the role of generalized Boltzmann weight factors, accounting for the modification of the discrete atomic states into continua through hybridization processes. We will see that the $a_N(\omega)$ functions always appear in combination with the impurity partition function Z_{f} in any measurable quantity, and thus there is an arbitrariness to the overall scale of the negative-frequency spectral functions in its definition. Note that the above NCA integral equations do not have $a_N(\omega)$ in them [a separate set of integral equations must be introduced for the a_N (Refs. 5, 6, and 43–46)]. In the numerical work, we calculate $a_N(\omega)$'s self-consistently.

The impurity partition function for our simple model is defined by

$$Z_{\mathrm{f}} \equiv \int d\omega[a_0(\omega)+2a_1(\omega)+2a_2(\omega)]. \tag{25}$$

This partition function includes the many-body effects of the interaction between the impurity and conduction band and is exact in form. We shall evaluate Z_{f} approximately with our solutions to the NCA integral equations.

In our simple model, only two kinds of conduction electron states are present: Γ_7 and Γ_8. Hybridization will mix the corresponding creation (destruction) operators with operators that create (destroy) f states of the same symmetry. The full measurable spectral functions of these f states are defined as a convolution of two neighboring configuration spectral functions, since to add or remove an f electron requires a change of configuration. It can be shown[5,6,43–46] that these measurable f-state spectral functions are given by

$$\rho_{\Gamma_7}(\omega) = \frac{1+e^{-\beta\omega}}{Z_{\mathrm{f}}}\int d\zeta a_0(\zeta)A_1(\zeta+\omega) = \rho_{01}(\omega), \tag{26}$$

$$\rho_{\Gamma_8}(\omega) = \frac{1+e^{-\beta\omega}}{Z_{\mathrm{f}}}\int d\zeta a_1(\zeta)A_2(\zeta+\omega) = \rho_{12}(\omega), \tag{27}$$

in this conserving approximation.[44] From now on, we will use the notation ρ_{01},ρ_{12} in favor of $\rho_{\Gamma_7},\rho_{\Gamma_8}$. This approximation does not include any vertex corrections.

From the leading bubble diagram,[6] the static magnetic susceptibility per Ce^{3+} impurity is

$$\chi(T) = \frac{1}{3}\mu_{\mathrm{eff}}^2\tilde{\chi}_{\mathrm{f}}(T), \quad \mu_{\mathrm{eff}}^2 = \frac{75}{49}\mu_{\mathrm{B}}^2, \tag{28}$$

$$\tilde{\chi}(T) = -\frac{4}{Z_{\mathrm{f}}}\int d\zeta a_1(\zeta,T)\mathrm{Re}G_1(\zeta,T). \tag{29}$$

Here μ_{B} is the Bohr magneton. The reduced dynamic magnetic susceptibility is

$$\tilde{\chi}''(\omega,T) = \frac{1-e^{-\beta\omega}}{Z_{\mathrm{f}}}\int d\zeta a_1(\zeta,T)A_1(\zeta+\omega,T). \tag{30}$$

Note that χ is a self-convolution within the $f^1\ \Gamma_7$ sector of states. This makes sense since any magnetic excitation must involve a change of state within that sector.

IV. ZERO-TEMPERATURE ANALYSIS

At zero temperature, it is possible to analyze the NCA integral equations analytically[14,48] to obtain a qualitative understanding of our model system. In particular, this may be used to compare with the conformal field theory approach[8] which calculated the operator scaling dimensions and critical behavior of physical properties in an asymptotically exact way $(T\rightarrow 0)$ for the multichannel Kondo exchange models with any size of impurity spin. In Ref. 14, an evaluation is given of the operator scaling dimensions and physical properties for the $SU(M)\times SU(N)$ multichannel Anderson, Coqblin-Schrieffer models using the functional integral formulation. The saddle point conditions for the model yield the NCA self-consistent integral equations. The simple exchange models become congruent with the $\mathrm{SU}(M)\times\mathrm{SU}(N)$ models when the impurity spin is $S_I=1/2$ $(N=2)$.

The main results of the zero-temperature analysis of the NCA integral equations for our model are as follows.

(1) We can find a criterion to assess whether the ground state will be that of the one-, two-, or three-channel model.

(2) The Kondo energy scale (T_0) can be estimated analytically for the case $\Gamma_{01}=\Gamma_{12}$. Here T_0 in the one- and two-channel model parameter regimes is shown to vanish as the $f^2\Gamma_3$ energy level approaches that of the f^0 configuration.

(3) We obtain the correct scaling dimensions for the overcompensated cases which agree with the conformal field theory results.[9]

(4) The crossover physics between the parameter regimes for different numbers of channels can be fully characterized.

The self-consistent NCA integral equations can be transformed into differential equations for the flat conduction band in the wideband limit: $D\gg|\epsilon_{1,2}|$. We analyze the zero-temperature NCA equations in the asymptotic limit $|\omega-E_0|\ll T_0$. Here E_0 is the threshold (ground-state) energy below which the pseudoparticle Green's functions become purely real. We introduce the inverse Green's functions and transform the self-energy equations at zero temperature into

coupled nonlinear differential equations,[48] given by

$$g_0(\omega)\equiv -1/G_0(\omega),\quad g_1(\omega)\equiv -1/G_1(\omega),\quad g_2(\omega)\equiv -1/G_2(\omega), \tag{31}$$

$$\frac{d}{d\omega}g_0(\omega)=-1-\frac{2\Gamma_{01}}{\pi}\frac{1}{g_1(\omega)},\quad g_0(-D)=D, \tag{32}$$

$$\frac{d}{d\omega}g_1(\omega)=-1-\frac{\Gamma_{01}}{\pi}\frac{1}{g_0(\omega)}-\frac{2\Gamma_{12}}{\pi}\frac{1}{g_2(\omega)},\quad g_1(-D)=D+\epsilon_1, \tag{33}$$

$$\frac{d}{d\omega}g_2(\omega)=-1-\frac{2\Gamma_{12}}{\pi}\frac{1}{g_1(\omega)},\quad g_2(-D)=D+\epsilon_2. \tag{34}$$

Note that we have included appropriate boundary conditions for these equations. Then g_0 and g_2 can be shown to be related by

$$\frac{g_2}{\Gamma_{12}}=\frac{g_0}{\Gamma_{01}}+\left[\frac{1}{\Gamma_{01}}-\frac{1}{\Gamma_{12}}\right](\omega-E_0)+\gamma_c, \tag{35}$$

$$\gamma_c=\frac{\epsilon_2-E_0}{\Gamma_{12}}+\frac{E_0}{\Gamma_{01}}. \tag{36}$$

In the zero-temperature analysis, it is more convenient to define the ''negative-frequency'' spectral functions by $a_i(\omega)\equiv e^{-\beta\omega}A_i(\omega)/Z_f$. These spectral functions vanish above the threshold energy E_0 and satisfy

$$\frac{d}{d\omega}[a_0(\omega)|g_0(\omega)|^2]=-\frac{2\Gamma_{01}}{\pi}a_1(\omega), \tag{37}$$

$$\frac{d}{d\omega}[a_1(\omega)|g_1(\omega)|^2]=-\frac{\Gamma_{01}}{\pi}a_0(\omega)-\frac{2\Gamma_{12}}{\pi}a_2(\omega), \tag{38}$$

$$\frac{d}{d\omega}[a_2(\omega)|g_2(\omega)|^2]=-\frac{2\Gamma_{12}}{\pi}a_1(\omega). \tag{39}$$

It can be shown from the above relations that

$$\frac{d}{d\omega}[a_0(\omega)g_0(\omega)+2a_1(\omega)g_1(\omega)+2a_2(\omega)g_2(\omega)]=a_0(\omega)+2a_1(\omega)+2a_2(\omega). \tag{40}$$

By integrating this equation from $\omega=-\infty$ to $\omega=E_0$, we find the additional relation

$$[a_0(\omega)g_0(\omega)+2a_1(\omega)g_1(\omega)+2a_2(\omega)g_2(\omega)]_{\omega=E_0}=1. \tag{41}$$

This identity will be useful in finding the asymptotic behavior of the ''negative-frequency'' spectral functions. As a corollary, we have another identity in the $\omega\to E_0$ limit,

$$\frac{a_0(\omega)|g_0(\omega)|^2}{\Gamma_{01}}=\frac{a_2(\omega)|g_2(\omega)|^2}{\Gamma_{12}}. \tag{42}$$

This relation can be proved by using the boundary condition at $\omega=E_0$. We calculate the physical atomic spectral functions and the dynamic magnetic susceptibility defined in Sec. IV using

$$\rho_{01}(\omega)=\int d\epsilon[a_0(\epsilon)A_1(\epsilon+\omega)+A_0(\epsilon)a_1(\epsilon+\omega)], \tag{43}$$

$$\rho_{12}(\omega)=\int d\epsilon[a_1(\epsilon)A_2(\epsilon+\omega)+A_1(\epsilon)a_2(\epsilon+\omega)], \tag{44}$$

$$\tilde{\chi}''(\omega)=\int d\epsilon[a_1(\epsilon)A_1(\epsilon+\omega)-A_1(\epsilon)a_1(\epsilon+\omega)]. \tag{45}$$

From the ω dependence of the spectral functions near $\omega=0$, we can infer the finite-temperature dependence of transport coefficients as will be discussed below.

We now discuss the phase diagram in the model parameter space using the zero-temperature analysis. The parameter γ_c decides the low-energy and low-temperature behaviors of our model Hamiltonian. γ_c measures the relative magnitude of the antiferromagnetic coupling strengths when the charge fluctuation is removed in the model Hamiltonian. Noting that $E_0\approx\epsilon_1+\mathcal{O}(V_{01}^2,V_{12}^2)$, we find

$$\gamma_c\approx\frac{2}{\pi N(0)}\left[\frac{1}{J_2}-\frac{1}{J_1}\right], \tag{46}$$

which illustrates the correspondence to the scaling analysis. If γ_c is greater than zero, divergent behavior shows up in the f^0 Green's function, and not in the f^2 Green's function. Hence the system will be dominated by the f^0 and f^1 sector, leading to the one-channel Kondo effect. When γ_c is less than zero, divergent behavior shows up in the f^2 Green's function, and not in the f^0 Green's function. In this case the f^1 and f^2 sector (two-channel Kondo physics) determines the low-temperature behavior of the system. When $\gamma_c=0$, f^0 and f^2 become equivalent asymptotically ($|\omega-E_0|\ll T_0$). Both Green's functions develop singular behaviors at the ground-state energy. In this model parameter regime, the three-channel Kondo model fixed point is realized at $T\to 0$.

The characteristic Kondo energy scale T_0 is found from an integration constant which connects the low- and high-energy states. We can obtain the integration constant for the case $\Gamma_{12}=\Gamma_{01}(=\Gamma)$. We will analyze this case in detail and indicate subsequently how to extend the zero-temperature analysis to the case of arbitrary relative hybridization strength.

A. Symmetric hybridization limit $\Gamma_{12}=\Gamma_{01}(=\Gamma)$

When we take the symmetric hybridization limit $\Gamma_{12}=\Gamma_{01}(=\Gamma)$, the $T=0$ NCA equations are simplified. In particular,

$$\gamma_c=\frac{\epsilon_2}{\Gamma}, \tag{47}$$

$$g_2=g_0+\epsilon_2, \tag{48}$$

$$a_0 g_0^2 = a_2 g_2^2. \tag{49}$$

The last two relations hold true in the asymptotic limit $|\omega - E_0| \ll T_0$. The ground state is determined solely by the sign of the f^2 configuration energy relative to the f^0 configuration energy. Removing the variable ω, we can find the differential equations between the inverse Green's functions. Integrating from the values at $\omega = -D$ to those at ω, we find the integration constant

$$\exp\left[\frac{\pi}{2\Gamma}[g_0 - g_1 + \epsilon_1]\right] = \left[\frac{g_1}{D}\right]\left[\frac{g_0}{D}\right]^{-1/2}\left[\frac{g_0+\epsilon_2}{D}\right]^{-1}. \tag{50}$$

This expression is valid in the wide conduction band limit $D \gg |\epsilon_{1,2}|$. We identify three cases for evaluating T_0.

(1) *One-channel case* $\gamma_c > 0$ or $\epsilon_2 > 0$. In this case the f^0 Green's function develops a divergent behavior at the threshold energy, while the f^2 Green's function does not. Thus the ground-state physics is dominated by the sector f^0-f^1, leading to the one-channel Kondo effect. The integration constant and the Kondo temperature are

$$\frac{g_1}{T_0} = \left[\frac{g_0}{\Delta}\right]^{1/2}\left[1 + \frac{g_0}{\epsilon_2}\right]\exp\left[\frac{\pi(g_0 - g_1)}{2\Gamma}\right], \tag{51}$$

$$T_0 = D\left[\frac{\epsilon_2}{D}\right]\left[\frac{\Gamma}{\pi D}\right]^{1/2}\exp\left[\frac{\pi\epsilon_1}{2\Gamma}\right]. \tag{52}$$

Here $\Delta \equiv \Gamma/\pi$. We can find the asymptotic behavior of the Green's functions for each atomic state as

$$\frac{g_0(\omega)}{\Delta} \approx \tilde{\Omega}^{\alpha_0}, \tag{53}$$

$$\frac{g_1(\omega)}{T_0} \approx \tilde{\Omega}^{\alpha_1}, \tag{54}$$

$$g_2(\omega) = g_0(\omega) + \epsilon_2, \tag{55}$$

$$\tilde{\Omega} = 3\frac{E_0 - \omega}{T_0}, \tag{56}$$

$$\alpha_0 = \tfrac{2}{3}, \quad \alpha_1 = \tfrac{1}{3}. \tag{57}$$

Although the scaling dimension is not correct (it leads to non-Fermi-liquid behavior in this single-channel model), the estimated Kondo temperature is correct within order unity and $\chi(0) \sim 1/T_0$ as expected for the one-channel model. An interesting observation is that the Kondo temperature vanishes as ϵ_2 tends to zero, i.e., as we approach the three-channel parameter regime (see the discussion below).

A detailed derivation of the asymptotic behavior is not included in this case since the NCA does not produce a Fermi-liquid fixed point in the one-channel model. We just give a brief summary of the zero-temperature analysis which is relevant to our study: $A_2(\omega)$ vanishes as $\tilde{\Omega}^{2/3}$ at the threshold energy, while A_0 (A_1) diverges as $\tilde{\Omega}^{-2/3}$ ($\tilde{\Omega}^{-1/3}$) as $\omega \to E_0$. Thus, the physical spectral function ρ_{12} vanishes as $|\omega|^{4/3}$ at the Fermi energy, while ρ_{01} is finite.

(2) *Two-channel case* $\gamma_c < 0$ or $\epsilon_2 < 0$. In contrast to the one-channel case, the f^2 spectral function has a divergent behavior at the threshold, leading to the two-channel ground state. The integration constant and the Kondo temperature are

$$\frac{g_1}{T_0} = \exp\left[\frac{\pi(g_2 - g_1)}{2\Gamma}\right]\left[1 + \frac{g_2}{|\epsilon_2|}\right]^{1/2}\frac{g_2}{\Delta}, \tag{58}$$

$$T_0 = D\left[\frac{|\epsilon_2|}{D}\right]^{1/2}\left[\frac{\Gamma}{\pi D}\right]\exp\left[\frac{\pi(\epsilon_1 - \epsilon_2)}{2\Gamma}\right]. \tag{59}$$

Note that the Kondo temperature vanishes with $\epsilon_2 \to 0$. We can find the asymptotic behavior following the standard zero-temperature analysis as

$$g_0(\omega) = g_2(\omega) + |\epsilon_2|, \tag{60}$$

$$\frac{g_1(\omega)}{T_0} = \tilde{\Omega}^{1/2}[1 + c_1\tilde{\Omega}^{1/2} + \mathcal{O}(\tilde{\Omega})], \tag{61}$$

$$\frac{g_2(\omega)}{\Delta} = \tilde{\Omega}^{1/2}[1 + c_2\tilde{\Omega}^{1/2} + \mathcal{O}(\tilde{\Omega})], \tag{62}$$

$$\tilde{\Omega} = 4\frac{E_0 - \omega}{T_0}, \tag{63}$$

$$c_1 = \frac{1}{6}\left[2\left(1 + \frac{\Delta}{|\epsilon_2|}\right) - \frac{T_0}{\Delta}\right], c_2 = -\frac{1}{6}\left[\left(1 + \frac{\Delta}{|\epsilon_2|}\right) - 2\frac{T_0}{\Delta}\right]. \tag{64}$$

The asymptotic behavior above the ground-state energy E_0 can be obtained from the expressions below E_0 by analytic continuation. Furthermore, we find for the ''negative-frequency'' spectra that

$$\frac{d}{d\tilde{\Omega}} a_0 g_0^2 = \frac{T_0\Delta}{2} a_1, \tag{65}$$

$$\frac{d}{d\tilde{\Omega}} a_1 g_1^2 = \frac{T_0\Delta}{2}[\tfrac{1}{2} a_0 + a_2], \tag{66}$$

$$\frac{d}{d\tilde{\Omega}} a_2 g_2^2 = \frac{T_0\Delta}{2} a_1, \tag{67}$$

which implies for $|\omega - E_0| \ll T_0$ that

$$a_0 = \frac{\Delta}{4|\epsilon_2|^2}\tilde{\Omega}^{1/2}[1 - x_0\tilde{\Omega}^{1/2} + \mathcal{O}(\tilde{\Omega})], \tag{68}$$

$$a_1 = \frac{1}{4T_0}\tilde{\Omega}^{-1/2}[1 - x_1\tilde{\Omega}^{1/2} + \mathcal{O}(\tilde{\Omega})], \tag{69}$$

$$a_2 = \frac{1}{4\Delta}\tilde{\Omega}^{-1/2}[1 - x_2\tilde{\Omega}^{1/2} + \mathcal{O}(\tilde{\Omega})], \tag{70}$$

$$x_0 = \frac{2}{3}(2c_1 + c_2) + 2\frac{\Delta}{|\epsilon_2|} = \frac{1}{3}\left(1 + \frac{7\Delta}{|\epsilon_2|}\right), \tag{71}$$

$$x_1 = \frac{4}{3}(2c_1 + c_2) = \frac{2}{3}\left(1 + \frac{\Delta}{|\epsilon_2|}\right), \tag{72}$$

$$x_2=\frac{4}{3}(c_1+2c_2)=\frac{2}{3}\frac{T_0}{\Delta}. \tag{73}$$

Note that $x_{0,1,2}>0$. Now we can find the asymptotic behavior of the pseudoparticle spectral functions as

$$A_0(\omega)=\frac{\Delta}{\pi|\epsilon_2|^2}\theta(\omega-E_0)[|\tilde{\Omega}|^{1/2}+\mathcal{O}(|\tilde{\Omega}|^{3/2})], \tag{74}$$

$$A_1(\omega)=\frac{1}{\pi T_0}\theta(\omega-E_0)[|\tilde{\Omega}|^{-1/2}+\mathcal{O}(|\tilde{\Omega}|^{1/2})], \tag{75}$$

$$A_2(\omega)=\frac{1}{\pi\Delta}\theta(\omega-E_0)[|\tilde{\Omega}|^{-1/2}+\mathcal{O}(|\tilde{\Omega}|^{1/2})]. \tag{76}$$

As expected, $A_0(\omega)$ vanishes at the threshold energy and does not develop any divergent behavior. On the other hand, $A_1(\omega)$ and $A_2(\omega)$ diverge at the threshold energy. Finally the physical spectral functions in the asymptotic limit $\omega\to 0$ are given by

$$\rho_{01}(\omega>0)=\frac{\Delta}{32|\epsilon_2|^2}\left[\tilde{\omega}-\frac{8x_0}{3\pi}\tilde{\omega}^{3/2}+\cdots\right], \tag{77}$$

$$\rho_{01}(\omega<0)=\frac{\Delta}{32|\epsilon_2|^2}\left[|\tilde{\omega}|-\frac{4x_1}{3\pi}|\tilde{\omega}|^{3/2}+\cdots\right], \tag{78}$$

$$\rho_{12}(\omega>0)=\frac{1}{16\Delta}\left[1-\frac{2x_1}{\pi}\sqrt{\tilde{\omega}}+\cdots\right], \tag{79}$$

$$\rho_{12}(\omega<0)=\frac{1}{16\Delta}\left[1-\frac{2x_2}{\pi}\sqrt{|\tilde{\omega}|}+\cdots\right], \tag{80}$$

$$\chi''(\omega)=\frac{\mathrm{sign}(\omega)}{16\Delta}\left[1-\frac{2x_1}{\pi}\sqrt{|\tilde{\omega}|}+\cdots\right], \tag{81}$$

$$\tilde{\omega}=4\frac{\omega}{T_0}. \tag{82}$$

$\rho_{01}(\omega)$ vanishes at $\omega=0$ and increases linearly in $|\omega|$ away from the Fermi level. This spectral depletion at the Fermi level is also confirmed in the finite-temperature NCA calculation. ρ_{12} is peaked right at the Fermi level and has more spectral weight below than above the Fermi level since $x_2<x_1$ for $T_0<\Delta$. The finite-temperature NCA results also confirm this observation. The spectral functions become nonanalytic at the Fermi level at zero temperature. Note that the dynamic magnetic susceptibility is step function like at $\omega=0$, which is none other than marginal Fermi liquid behavior.[14]

From the asymptotic form of the zero-temperature spectral functions, we can infer the finite-temperature dependence of the resistivity using the Kubo formula

$$\frac{1}{\rho(T)}=\frac{ne^2}{m}\int d\omega\,\tau(\omega)\left(-\frac{\partial f}{\partial\omega}\right). \tag{83}$$

For $\omega,T\ll T_0$, the relaxation rate for the conduction electron is approximately

$$\frac{1}{\tau(\omega)}\propto\rho_{12}(\omega,T). \tag{84}$$

Near zero temperature, we may replace $\rho_{12}(\omega,T)$ by our zero-temperature one and find the $\sqrt{T}$ temperature dependence. A complication arises here due to angular averaging. Since the angular harmonic conjugate to ρ_{12} is positive definite, still the above simple argument applies; that is, the anisotropy will not affect the conclusion of the low-temperature NCA analysis. Hence, we expect, for $M=2,3$, that the calculated scaling dimensions will agree with those obtained from conformal theory. In the one-channel case, the important angular harmonic (which multiplies ρ_{01}) is not positive definite and we cannot straightforwardly carry over the low-T NCA analysis to an understanding of the low-temperature resistivity as the angular average can modify the sign of the low-T coefficients. However, since the $T\to 0$ physics must be Fermi-liquid-like for $M=1$, which the NCA cannot correctly produce, this difficulty is rendered practically academic.

We summarize the low-temperature properties as follows.

(i) The atomic spectral function ρ_{12} is peaked right at the Fermi level, independent of the occupancy, while ρ_{01} vanishes at $\omega=0$ and is depleted near the Fermi level.

(ii) The dynamic magnetic susceptibility is step-function-like at zero frequency.

(iii) The resistivity obeys the scaling behavior $\rho(T)=\rho(0)[1-a\sqrt{T/T_0}]$ near zero temperature.

All these results are consistent with numerical NCA calculations at finite temperatures.

(3) *Three-channel case* $\gamma_c=0$ or $\epsilon_2=0$. In this case, the f^0 and f^2 configurations produce asymptotically equivalent spectra that give rise to a three-channel Kondo model ground state. The integration constant and the Kondo temperature are

$$\frac{g_1}{T_0}=\left[\frac{g_0}{\Delta}\right]^{3/2}\exp\left[\frac{\pi}{2\Gamma}(g_0-g_1)\right], \tag{85}$$

$$T_0\approx D\left[\frac{\Gamma}{\pi D}\right]^{3/2}\exp\left[\frac{\pi\epsilon_1}{2\Gamma}\right]. \tag{86}$$

See Appendix B for a detailed derivation of the asymptotic behavior. This model case is not different from the analysis of the general overcompensated models. We simply list the asymptotic behavior here as

$$g_0(\omega)=g_2(\omega), \tag{87}$$

$$\frac{g_1(\omega)}{T_0}=\tilde{\Omega}^{3/5}[1+c_1\tilde{\Omega}^{2/5}+d_1\tilde{\Omega}^{3/5}+\cdots], \tag{88}$$

$$\frac{g_2(\omega)}{\Delta}=\tilde{\Omega}^{2/5}[1+c_2\tilde{\Omega}^{2/5}+d_2\tilde{\Omega}^{3/5}+\cdots], \tag{89}$$

$$\tilde{\Omega}=5\frac{E_0-\omega}{T_0}, \tag{90}$$

$$c_1=\frac{2}{7},\quad d_1=-\frac{T_0}{8\Delta},\quad c_2=-\frac{1}{7},\quad d_2=\frac{T_0}{4\Delta}. \tag{91}$$

The negative-frequency spectral functions are given by

$$a_1(\omega)=\frac{1}{5T_0}\widetilde{\Omega}^{-3/5}[1-x_1\widetilde{\Omega}^{2/5}-y_1\widetilde{\Omega}^{3/5}+\cdots]\theta(\widetilde{\Omega}), \tag{92}$$

$$a_2(\omega)=\frac{1}{5\Delta}\widetilde{\Omega}^{-2/5}[1-x_2\widetilde{\Omega}^{2/5}-y_2\widetilde{\Omega}^{3/5}+\cdots]\theta(\widetilde{\Omega}), \tag{93}$$

$$x_1=2c_1=\frac{4}{7},\quad y_1=0,\quad x_2=0,\quad y_2=2d_2=\frac{T_0}{2\Delta}, \tag{94}$$

and the pseudoparticle spectral functions are

$$A_1(\omega)=\frac{\sin(3\pi/5)}{\pi T_0}|\widetilde{\Omega}|^{-3/5}[1-x_1\cos(2\pi/5)|\widetilde{\Omega}|^{2/5}+\cdots]\times\theta(-\widetilde{\Omega}), \tag{95}$$

$$A_2(\omega)=\frac{\sin(2\pi/5)}{\pi\Delta}|\widetilde{\Omega}|^{-2/5}[1-y_2\cos(2\pi/5)|\widetilde{\Omega}|^{3/5}+\cdots]\times\theta(-\widetilde{\Omega}). \tag{96}$$

From the pseudoparticle spectral functions, we can find the physical spectral functions in the asymptotic limit of $\omega\rightarrow E_0$, and they are given by

$$\rho_{01}(\omega)=\rho_{12}(-\omega), \tag{97}$$

$$\rho_{12}(\omega>0)=\frac{\sin(2\pi/5)}{25\pi\Delta}[B(2/5,3/5)-x_1B(3/5,4/5)|\widetilde{\omega}|^{2/5}-y_2\cos(2\pi/5)B(2/5,6/5)|\widetilde{\omega}|^{3/5}+\cdots], \tag{98}$$

$$\rho_{12}(\omega<0)=\frac{\sin(3\pi/5)}{25\pi\Delta}[B(2/5,3/5)-x_1\cos(2\pi/5)B(3/5,4/5)|\widetilde{\omega}|^{2/5}-y_2B(2/5,6/5)|\widetilde{\omega}|^{3/5}+\cdots], \tag{99}$$

$$\widetilde{\chi}''(\omega)=\mathrm{sign}(\omega)\frac{\sin(3\pi/5)}{25\pi T_0}\{B(2/5,2/5)|\widetilde{\omega}|^{-1/5}-x_1[1+\cos(2\pi/5)]B(2/5,4/5)|\widetilde{\omega}|^{1/5}+\cdots\}, \tag{100}$$

$$\widetilde{\omega}=5\frac{\omega}{T_0}. \tag{101}$$

Here $B(p,q)$ is the β function. The spectral functions become nonanalytic at the Fermi level at zero temperature. One important observation is that the power laws agree with those obtained from conformal field theory treatments for the overcompensated three-channel $S_I=1/2$ models. Since ρ_{01} and ρ_{12} are equivalent in the asymptotic limit, the angular functions are factored out in the conduction electron scattering time. Thus we can read off the power law of the resistivity, $\alpha=2/5$.

The low-temperature properties are summarized as follows.

(i) The atomic spectral function is peaked right at the Fermi level, independent of the occupancy.

(ii) The dynamic magnetic susceptibility diverges as $\omega^{-1/5}$ at zero frequency.

(iii) The resistivity obeys the scaling behavior $\rho(T)=\rho(0)[1-a(T/T_0)^{0.4}]$ near zero temperature, which is consistent with numerical NCA calculations at finite T.

B. Crossover physics

We expect a smooth crossover from the high-temperature regime to the low-temperature regime where the calculation will settle to the fixed point for one of $M=1,2,3$ channels. We can estimate the crossover temperature in the one- and two-channel model parameter regime using the zero-temperature analysis. This follows from the fact that in the asymptotic analysis we have $g_0\ll\epsilon_2$ for the one-channel regime and $g_2\ll|\epsilon_2|$ for the two-channel regime (see the integration constant). In the one-channel case, the integration constant can be rewritten as

$$\frac{g_1}{T_0^{(3)}}=\left[1+\frac{\epsilon_2}{g_0}\right]\left[\frac{g_0}{\Delta}\right]^{3/2}\exp\left[\frac{\pi(g_0-g_1)}{2\Gamma}\right]. \tag{102}$$

We can see that the relative magnitude of g_0 and ϵ_2 determines the fixed-point behavior. The crossover energy scale between high temperatures (three channels) and low temperatures (one channel) can be defined by the relation $g_0=\epsilon_2$. The crossover temperature is found in the one-channel case to be

$$T_x^{(1)}=\frac{T_0}{3}\left[\frac{\epsilon_2}{\Delta}\right]^{3/2}. \tag{103}$$

In the two-channel case, using similar reasoning, we find the crossover temperature to be

$$T_x^{(2)}=\frac{T_0}{4}\left[\frac{|\epsilon_2|}{\Delta}\right]^{2}. \tag{104}$$

Substituting the Kondo energy scale into the above expressions, we can see that the crossover energy scales are given by

$$T_x^{(1)}=\frac{1}{3}\left[\frac{\epsilon_2}{\Delta}\right]^{5/2}D\left[\frac{\Gamma}{\pi D}\right]^{3/2}\exp\left[\frac{\pi\epsilon_1}{2\Gamma}\right], \tag{105}$$

$$T_x^{(2)}=\frac{1}{4}\left[\frac{|\epsilon_2|}{\Delta}\right]^{5/2}D\left[\frac{\Gamma}{\pi D}\right]^{3/2}\exp\left[\frac{\pi(\epsilon_1-\epsilon_2)}{2\Gamma}\right]. \tag{106}$$

Note that each crossover temperature vanishes as $|\epsilon_2|^{5/2}$ with $\epsilon_2\rightarrow 0$. We intentionally write the crossover temperature as the prefactor times the corresponding three-channel Kondo temperature. If this prefactor is greater than 1, the system will not display three-channel behavior with decreasing temperatures but will flow directly to the one- or two-channel fixed point. When this prefactor is less than 1, the system will display three-channel behavior before finally flowing to the lower-temperature fixed point.

TABLE I. Model parameters for the Ce impurity. This set of model parameters covers the single, three-, and two-channel Kondo regimes. $\Gamma=\Gamma_{01}=\Gamma_{12}$ is the hybridization strength for both f^0-f^1 and f^1-f^2 mixing, respectively. We scan the channel number $M=1,2,3$ according to whether $\epsilon_2>0,<0,=0$. The Kondo scale T_0 is estimated as described in the text.

Set	M	Γ/D	ϵ_1/D	ϵ_2/D	k_BT_0/D
1	2	0.2	−0.4	−0.1	1.9081×10^{-3}
2	2	0.2	−0.37	−0.07	1.5964×10^{-3}
3	2	0.2	−0.35	−0.05	1.3492×10^{-3}
4	3	0.2	−0.3	0.0	1.5224×10^{-3}
5	3	0.2	−0.4	0.0	6.9413×10^{-3}
6	1	0.2	−0.3	0.05	1.1957×10^{-3}
7	1	0.2	−0.3	0.07	1.6740×10^{-3}
8	1	0.2	−0.3	0.10	2.3914×10^{-3}

C. General asymmetric hybridization case

Though the Kondo energy scale cannot be estimated analytically for the general case $\Gamma_{01}\neq\Gamma_{12}$, the asymptotic behavior ($\omega\to E_0$) can be still be sorted out. Since the physics is the same as in the above analysis, we shall just write the asymptotic properties of Green's functions for the three relevant cases.

(1) $\gamma_c>0$:

$$g_0(\omega)\approx\frac{\Gamma_{01}}{\pi}\left[3\frac{E_0-\omega}{T_0}\right]^{\alpha_0}, \tag{107}$$

$$g_1(\omega)\approx T_0\left[3\frac{E_0-\omega}{T_0}\right]^{\alpha_1}, \tag{108}$$

$$g_2(\omega)=\frac{\Gamma_{12}}{\Gamma_{01}}g_0(\omega)+\left[\frac{\Gamma_{12}}{\Gamma_{01}}-1\right](\omega-E_0)+\gamma_c\Gamma_{12}, \tag{109}$$

$$\alpha_0=\tfrac{2}{3},\quad \alpha_1=\tfrac{1}{3}. \tag{110}$$

(2) $\gamma_c<0$:

$$g_0(\omega)=\frac{\Gamma_{01}}{\Gamma_{12}}g_2(\omega)+\left[\frac{\Gamma_{01}}{\Gamma_{12}}-1\right](\omega-E_0)+|\gamma_c|\Gamma_{01}, \tag{111}$$

$$g_1(\omega)\approx T_0\left[4\frac{E_0-\omega}{T_0}\right]^{\alpha_1}, \tag{112}$$

$$g_2(\omega)\approx\frac{\Gamma_{12}}{\pi}\left[4\frac{E_0-\omega}{T_0}\right]^{\alpha_2}, \tag{113}$$

$$\alpha_1=\tfrac{1}{2},\quad \alpha_2=\tfrac{1}{2}. \tag{114}$$

(3) $\gamma_c=0$: In this case, f^0 and f^2 are equivalent asymptotically as $\omega\to E_0$,

$$g_2(\omega)=\frac{\Gamma_{12}}{\Gamma_{01}}g_0(\omega)+\left[\frac{\Gamma_{12}}{\Gamma_{01}}-1\right](\omega-E_0), \tag{115}$$

$$\frac{d}{d\omega}g_0(\omega)=-1-\frac{2\Gamma_{01}}{\pi}\frac{1}{g_1(\omega)},\quad g_0(-D)=D, \tag{116}$$

$$\frac{d}{d\omega}g_1(\omega)=-1-\frac{\Gamma_{01}}{\pi}\left[\frac{1}{g_0(\omega)}+\frac{2}{g_0(\omega)+(1-\Gamma_{01}/\Gamma_{12})(\omega-E_0)}\right],\quad g_1(-D)=D+\epsilon_1. \tag{117}$$

Then the asymptotic form follows:

$$g_0(\omega)\approx\frac{\Gamma_{01}}{\pi}\left[5\frac{E_0-\omega}{T_0}\right]^{\alpha_0}, \tag{118}$$

$$g_1(\omega)\approx T_0\left[5\frac{E_0-\omega}{T_0}\right]^{\alpha_1}, \tag{119}$$

$$\alpha_0=\tfrac{2}{5},\quad \alpha_1=\tfrac{3}{5}. \tag{120}$$

Though the Kondo energy scale cannot be evaluated analytically, it can be estimated from the numerical NCA calculation of, e.g., the magnetic susceptibility and by then performing a scaling analysis over a set of parameter values.

V. NUMERICAL ANALYSIS

In this section we present results from our full numerical study at finite temperatures. We studied the model for the parameters listed in Table I. This covers the one-, two-, and three-channel Kondo regimes. For simplicity, we have chosen the same hybridization strength in the f^0-f^1 and f^1-f^2 sectors. The relevant physics associated with the $M=1,2,3$ channel fixed points can then be studied by varying the relative position of the f^0 and f^2 configuration energies. This simple choice of the hybridization further makes it possible to find the characteristic Kondo energy scales analytically, as we described in the previous section in detail.

Our main results are the following.

(1) The magnetic susceptibility shows a scaling behavior and agrees well with exact Bethe ansatz results in the two- and three-channel parameter regimes.

(2) The NCA results for the residual entropy in the two- and three-channel models agree with the exact ones to within about 5%, consistent with the expected order-$(1/N^2)$ corrections. The Kondo anomaly peak in the specific heat also agrees with the exact one in its magnitude.

(3) The thermopower is a diagnostic to display the ground states for different numbers of relevant channels for our model—this data has already been presented in Ref. 16 and will be only briefly discussed here.

(4) The dynamic magnetic susceptibility varies significantly between the compensated one-channel limit of our model and the overcompensated (two- and three-channel) limit of our model.

(5) Due to the simplifying features of our model, the resistivity shows a bendover at low temperatures in the one-channel parameter regime. The resistivity in the two- and three-channel parameter regimes shows temperature dependences near $T=0$ K in agreement with conformal field theory results.

(6) We have confirmed in detail that the NCA is a valid numerical self-consistent nonperturbative method in studying the overcompensated multichannel $S_I=1/2$ Anderson model at $T>0$.

A. Entropy and specific heat

The entropy and specific heat due to the magnetic impurity can be calculated from the free energy obtained in the NCA through numerical differentiation. These thermodynamic quantities include very important information about the nature of the ground state. We can estimate the characteristic energy scales in the Kondo models from the temperature variation of the entropy. In general, the entropy will increase with increasing temperatures, until the frozen impurity degrees of freedom are released. Our model Hamiltonian is expected to have entropy $S=k_B\ln 5$ at high enough temperatures, an intermediate regime with entropy $k_B\ln 2$ once the f^0 and f^2 configurations are frozen out, and a residual entropy for the $M=2,3$ limits of the model.

The entropy and the specific heat are displayed in Figs. 6 and 7 for the model parameter sets studied here. In the one-channel case, the Kondo anomaly peak is well separated from the Schottky anomaly peak coming from the interconfiguration excitations. The Kondo anomaly peak has a magnitude comparing well with the exact results[13] for the Kondo exchange model. No residual entropy remains with $T\to 0$. In the two-channel case, the Kondo anomaly peak is not clearly separated from the charge fluctuation peak for most of our model parameters. The residual entropy agrees within 5% with the exact one[13] and the discrepancy can be explained by the $\mathcal{O}(1/N^2)$ and higher-order corrections. To see this, we note that the entropy for spin-1/2 conduction electrons has an explicit dependence on the impurity spin degeneracy.[8,9] Strictly speaking, the NCA results are valid for N-fold impurity spin and M-fold channel degeneracies as $N\to\infty$ with N/M fixed. Hence it is natural to expect $\mathcal{O}(1/N^2)$ corrections to the entropy through the neglected vertex corrections. In the three-channel case, the Kondo anomaly peak is reduced further due to the increased residual entropy and is almost merged with the charge fluctuation contribution for model set 4. For model set 5, we can see a weak indication of separation. The residual entropy is increased compared to that of the two-channel case and its magnitude is again a little bit smaller than the exact one[13] due to the neglect of the higher-order contribution in the $1/N$ expansion.

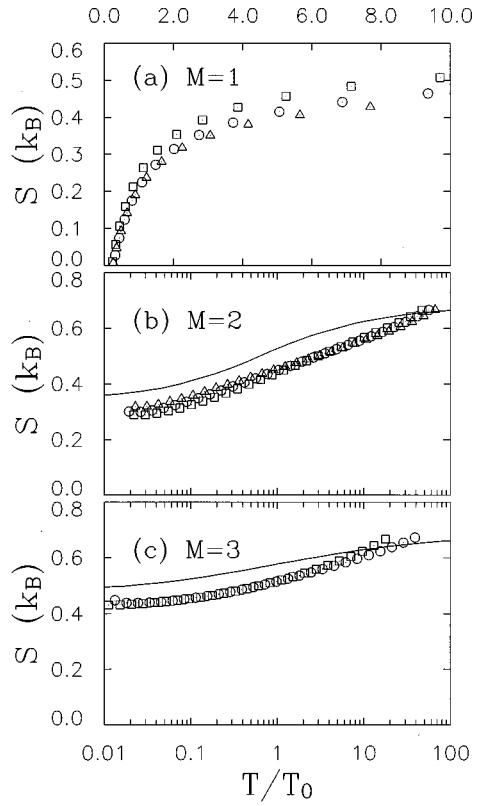

FIG. 6. Channel dependence of the entropy. The NCA calculation of entropy clearly shows the right magnitude of residual entropy depending on the relevant channel numbers. Solid lines are Bethe ansatz curves. Note that the temperature scale is linear for $M=1$. Referring to Table I: (a) $M=1$ case, □ for model set 8; ○ for model set 7; △ for model set 6. (b) $M=2$ case, □ for model set 1; ○ for model set 2; △ for model set 3. (c) $M=3$ case, □ for model set 4; ○ for model set 5.

B. Static magnetic susceptibility

The static magnetic susceptibility is a direct indicator of the nature of the ground state for the magnetic Kondo model. As is well documented, the magnetic susceptibility diverges logarithmically, $\chi(T)\propto\ln(T_0/T)$, for the two-channel $S_I=1/2$ magnetic Kondo model as $T\to 0$, and diverges algebraically for the three, viz., or the $M>2$, $S_I=1/2$ multichannel Kondo model ($\chi(T)\propto[T_0/T]^{1-2\Delta_n}$; $\Delta_n=2/(n+2)$, where n is the channel number (≥ 3)).[8,9,13] The one-channel Kondo model has a constant magnetic susceptibility at zero temperature [$\chi(0)\sim 1/T_0$]. From the NCA, using the leading-order bubble diagram,[6] the magnetic susceptibility for one Ce^{3+} impurity is given by

$$\chi(T)=\tfrac{1}{3}\mu_{\rm eff}^2\tilde{\chi}(T),\quad \mu_{\rm eff}^2=\tfrac{75}{49}\mu_{\rm B}^2, \tag{121}$$

$$\tilde{\chi}(T)=-\frac{4}{Z_f}\int d\zeta a_1(\zeta,T)\mathrm{Re}G_1(\zeta,T). \tag{122}$$

Here $\mu_{\rm B}$ is the Bohr magneton.

Our numerical results for $\tilde{\chi}(T)$ clearly show the right tendency for each possible low-T fixed point. The magnetic susceptibility in the one-channel regime, for model parameter sets 6, 7, and 8, shows approximate scaling behavior and clearly has negative curvature at low temperatures, indicat-

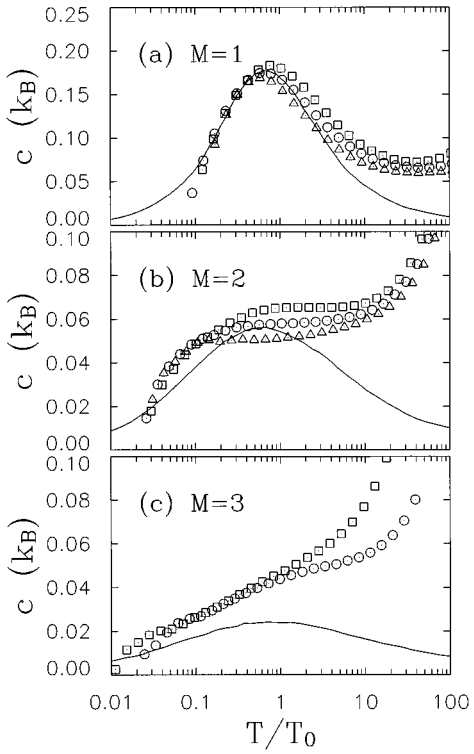

FIG. 7. Channel dependence of the specific heat. Solid lines are Bethe ansatz results. The comparison to the Bethe ansatz is complicated by the background derived from the interconfiguration peak. In the $M=1$ cases, the Kondo temperatures are adjusted such that the NCA numerical results fall on the exact Bethe ansatz one. Thoughout all the figures presented in this paper the estimated Kondo temperatures in the one-channel models are used except for the magnetic susceptibility curves (see Fig. 8). Symbols have the same meaning as in Fig. 6.

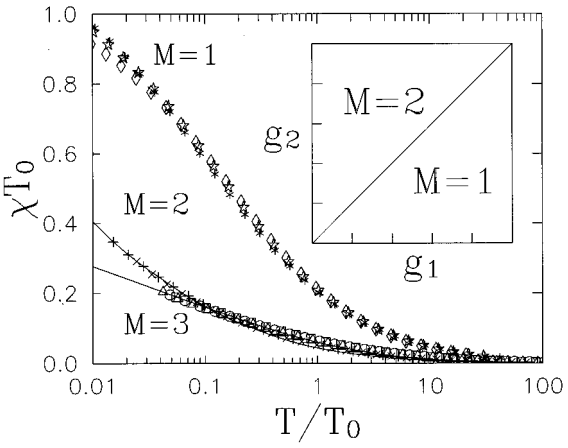

FIG. 8. The scaling behavior of the static magnetic susceptibility. The static magnetic susceptibility obeys a scaling behavior for each parameter regime, leading to the $M=1,2,3$ fixed points. The agreement with the Bethe ansatz results (solid lines) is good for the overscreened cases ($M=2,3$). $T_0=T_K/0.3$ for $M=2$, T_K from Ref. 13. $M=1$ case, $\diamond$ for model set 8; $\star$ for model set 7; * for model set 6. $M=2$ case, $\square$ for model set 1; $\bigcirc$ for model set 2; $\triangle$ for model set 3. $M=3$ case, + for model set 4; $\times$ for model set 5. The ground-state phase diagram for the model in exchange coupling constant parameter space is drawn in the inset, where $g_i=N(0)J_i$, $N(0)$ being the conduction band density of states at the Fermi energy. The solid diagonal line is for $M=3$.

ing an approach to the Fermi-liquid ground state. The deviation of the scaling behavior at low temperatures seems to come from the pathological behavior of the NCA in this one-channel case.[48]

The $\tilde{\chi}(T)$ curves in the two-channel regime, for the model parameter sets 1, 2, and 3, also show scaling behavior and diverge logarithmically at low temperatures (Fig. 8). Our results are compared with those of Ref. 13. The fitting to the exact Bethe ansatz numerical results[13] is quite good. We believe that the high-temperature deviation comes from the $M=3$ to $M=2$ crossover physics described in the previous section. Note that Bethe ansatz results are for the pure two-channel s-d exchange model. To get the fitting to the Bethe ansatz, we slide the temperature axis to find $T_K=0.3T_0$ (T_K from the Bethe ansatz). Here T_0 is the Kondo energy scale estimated from the zero-temperature analysis.

At high temperatures we cannot distinguish between the different possible fixed points so readily as in the low-temperature case. Note that distinct physics of the $M=1,2,3$ channel fixed points shows up at low temperatures below the crossover temperature which was estimated in the previous section. This observation is supported by results from the three-channel model parameter sets. The high-temperature deviation from scaling is very weak in this case which will not show the crossover physics. The magnetic susceptibility in the three-channel model also shows a scaling behavior. Since the three-channel case lies exactly on the boundary between the one-channel and two-channel regimes, we probed the three-channel case by varying the position of the bare f^1 configuration energy while the two excited configurations f^0, f^2 energies are kept equal. The fitting of the susceptibility to the exact results is quite good. The Kondo energy scale T_0 estimated from the zero-temperature analysis agrees with that in the exact Bethe ansatz (T_K of Ref. 13).

C. Spectral functions

The interconfiguration spectral functions show a distinct behavior for the $M=1,2,3$ fixed points in the energy region close to the Fermi level ($\omega=0$) depending on the model parameters. In our simple model, we have two atomic spectral functions for local f-creation operators of symmetry Γ_7 and Γ_8, $\rho_{\Gamma_7}(\omega)=\rho_{01}(\omega)$ and $\rho_{\Gamma_8}(\omega)=\rho_{12}(\omega)$, which are given by

$$\rho_{01}(\omega)=\frac{1+e^{-\beta\omega}}{Z_f}\int d\zeta e^{-\beta\zeta}A_0(\zeta)A_1(\zeta+\omega), \quad (123)$$

$$\rho_{12}(\omega)=\frac{1+e^{-\beta\omega}}{Z_f}\int d\zeta e^{-\beta\zeta}A_1(\zeta)A_2(\zeta+\omega). \quad (124)$$

In the one-channel model parameter regime (see Fig. 9), $\rho_{01}(\omega)$ develops the Kondo resonance peak just above the Fermi level and $\rho_{12}(\omega)$ is depleted near $\omega=0$ and tends to zero with $T\to 0$ at $\omega=0$. This confirms our zero-temperature analysis in Sec. IV. For comparison, note that the Kondo resonance amplitude is large compared to the two-channel or three-channel case.

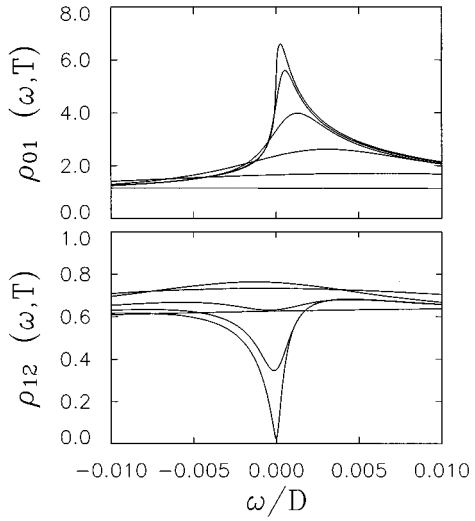

FIG. 9. Atomic spectral functions in the one-channel regime. ρ_{01} is the interconfiguration spectral function which is obtained from the convolution between f^0 and $f^1\Gamma_7$ states. ρ_{12} is the interconfiguration spectral function which is obtained from the convolution between $f^1\Gamma_7$ and $f^2\Gamma_3$ states. The one-channel Kondo effect leads to the Kondo resonance development in ρ_{01} just above the Fermi level and the spectral depletion in ρ_{12} right at $\omega=0$. Spectral functions are displayed for model set 8. In ascending order of the low-energy curves, the temperatures of the calculations are $T/D=3.678\times10^{-2}$, 1.077×10^{-2}, 3.155×10^{-3}, 9.239×10^{-4}, 2.706×10^{-4}, 7.924×10^{-5}.

In the two-channel regime (see Fig. 10), $\rho_{12}(\omega)$ is peaked below $\omega=0$ and its peak position tends to $\omega=0$ with decreasing temperature. Note that the Kondo resonance amplitude is reduced compared to the one-channel Kondo resonance amplitude. On the other hand, $\rho_{01}(\omega)$ is depleted near $\omega=0$.

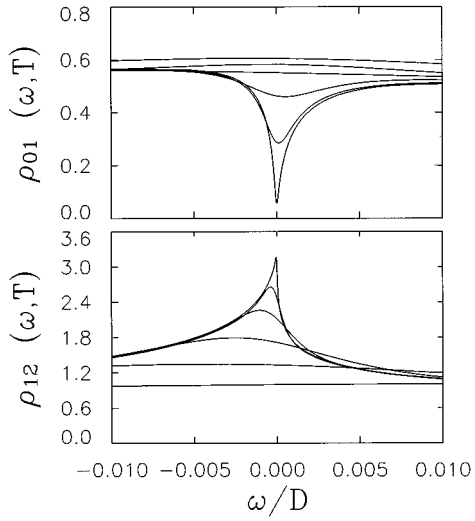

FIG. 10. Atomic spectral functions in the two-channel regime. The two-channel Kondo effect leads to the Kondo resonance development in ρ_{12} at the Fermi level ($T=0$) and the spectral depletion in ρ_{01} right at $\omega=0$. Spectral functions are displayed for model set 1. The temperature set is the same as in Fig. 9.

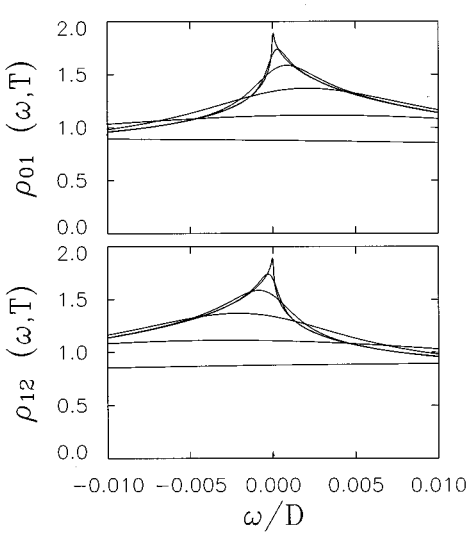

FIG. 11. Atomic spectral functions in the three-channel regime. For this parameter regime (model set 4), two spectral functions are equivalent in the asymptotic limit after a particle-hole transformation. The temperature set is the same as in Fig. 9.

In the three-channel parameter regime (see Fig. 11), the two spectral functions are equivalent asymptotically when the $\omega\rightarrow-\omega$ transformation is accounted for. The peak position of the resonance tends to zero with decreasing temperature.

As mentioned above, the positions of the Kondo resonance peak (see Fig. 12) show a distinct behavior for different $T\rightarrow0$ fixed points. The peak position saturates to a constant value in the one-channel case while it vanishes in the two- and three-channel cases with decreasing temperature. In addition, the detailed functional form of the Kondo resonance peak varies with the fixed-point channel number. In the overscreened cases ($M=2,3$), the peak structure becomes nonanalytic with decreasing temperature as shown in the zero-temperature analysis of the NCA integral equations. A finite temperature washes out this nonanalytic behavior at the Kondo resonance peak. In the one-channel case, exact results show that the correct atomic spectral functions must remain analytic down to zero temperature.

Since we are not considering all the atomic energy levels, the full atomic spectral functions (measured from the photoemission experiments) cannot be defined in our simple model. Although the high-energy physics of real systems cannot be properly treated within our simple model Hamiltonian, the low-energy or low-temperature properties can be studied using the restricted spectral functions. Note that low-temperature and low-energy physics is governed by the Kondo resonance peak in the spectra. Though a spectral depletion is found in the interconfiguration spectral functions, we do not expect that the photoemission spectroscopy can observe this feature unless it can distinguish the atomic electron symmetry. Also, it is not clear that this feature is realistic for the single-channel model. Measurable atomic spectral functions are shown in Fig. 13 for parameters yielding the $M=1,2,3$ fixed points.

D. Dynamic magnetic susceptibility

The dynamic magnetic susceptibility measures the magnetic excitation structure. Since the properties of the mag-

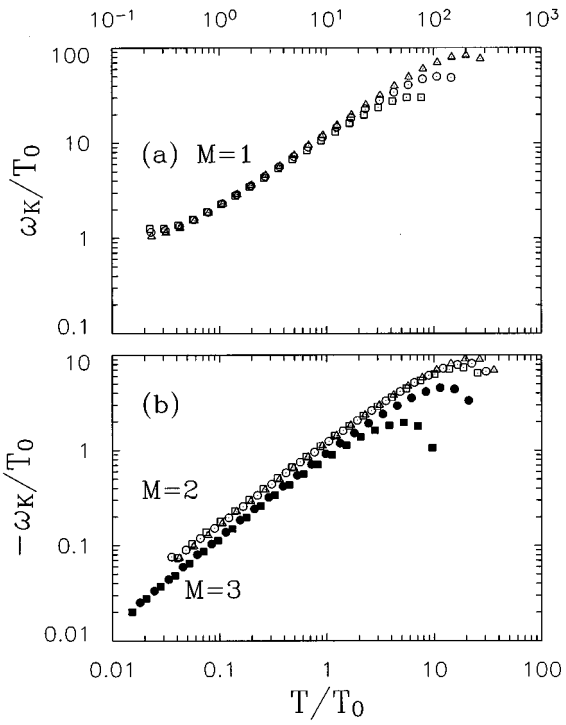

FIG. 12. Temperature dependence of the Kondo resonance peak. The Kondo resonance peak position (ω_K) shows a different temperature dependence for different numbers of channels. (a) One-channel case (ρ_{01}): ω_K decreases and saturates to a constant with decreasing temperature. (b) Two-channel case (ρ_{12}) and (c) three-channel case (ρ_{12}): ω_K decreases and tends to zero with decreasing temperature. Symbols have the same meaning as in Fig. 6 ($M=3$, solid square for model set 4; solid circle for model set 5). Note the different temperature ranges between $M=1$ case (top) and $M=2,3$ cases (bottom).

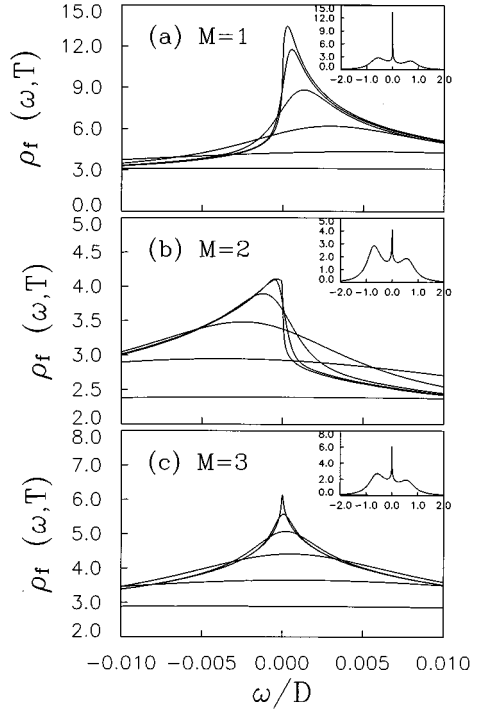

FIG. 13. Total atomic spectral function. The high-energy structure (insets) essentially does not depend on the temperature. On the other hand, the temperature and relevant channel number dependence show up in the Kondo resonance structure. (a) One-channel case (model set 8). (b) Two-channel case (model set 1). (c) Three-channel case (model set 4). The temperature set is the same as in Fig. 9.

netic excitations are related to the interaction of the local magnetic moment with the conduction electrons, the channel number at the fixed point will determine the nature of the magnetic excitations. The dynamic magnetic susceptibility is expected to be strongly dependent upon the value of M. We have already seen this channel number dependence in the static magnetic susceptibility.

The dynamic magnetic susceptibility is defined as the spin-spin correlation function and can be measured directly from neutron scattering experiments. From the leading bubble diagram, the reduced dynamic magnetic susceptibility is estimated as (neglecting conduction electron only and mixed conduction-f contributions which are expected to be down by at least lnD/D)

$$\tilde{\chi}''(\omega,T)=\frac{1-e^{-\beta\omega}}{Z_f}\int d\zeta a_1(\zeta,T)A_1(\zeta+\omega,T). \quad (125)$$

Our reduced static magnetic susceptibility is related to the above magnetic response function by the Kramer-Kronig relation

$$\tilde{\chi}(T)=2\int\frac{d\omega}{\pi}\frac{\tilde{\chi}''(\omega,T)}{\omega}. \quad (126)$$

The neutron scattering experiments measure the structure function $S(\omega,T)\propto[b(\omega)+1]\chi''(\omega,T)$.

The dynamic susceptibility can be quantitatively characterized by its ''linewidth'' dependence on temperature in addition to its overall functional shape. We may define the linewidth $\Gamma(T)$ by the peak position of $\chi''(\omega,T)$, which can be measured directly in inelastic neutron scattering experiments.

The variation of $\tilde{\chi}''(\omega,T)$ and $\Gamma(T)$ with temperature is displayed in Figs. 14 and 15. For the dynamic magnetic susceptibility, we display $\tilde{\chi}''(\omega,T)$ as a function of ω/T_0 and the reduced form $\tilde{\chi}''(\omega,T)/\tilde{\chi}''(\Gamma(T),T)$ (inset) as a function of $\omega/\Gamma(T)$ in Fig. 14. A distinct behavior for the different fixed points is clearly evidenced: In the one-channel regime, the $\tilde{\chi}''(\omega,T)$ curves converge with decreasing temperatures. This is clearly supported by the saturation of $\Gamma(T)$ at low temperatures. In the two- and three-channel regimes, $\Gamma(T)$ vanishes algebraically (close to linear) and the dynamic magnetic susceptibility does not converge in contrast to the one-channel case, but instead develops nonanalytic behavior at $\omega=0$. The reduced dynamic magnetic susceptibilities (defined above; see inset in Fig. 14) show an approximate scaling behavior between two extrema.

The physics of the magnetic linewidth is quite important in understanding the nature of the magnetic spin screening. Below T_0, changing the number of channels gives very different behavior. The impurity spin-flipping time (τ_f) due to the hybridization will be given by the inverse of the linewidth, $\tau_f\sim 1/\Gamma(T)$. On the other hand, thermally excited

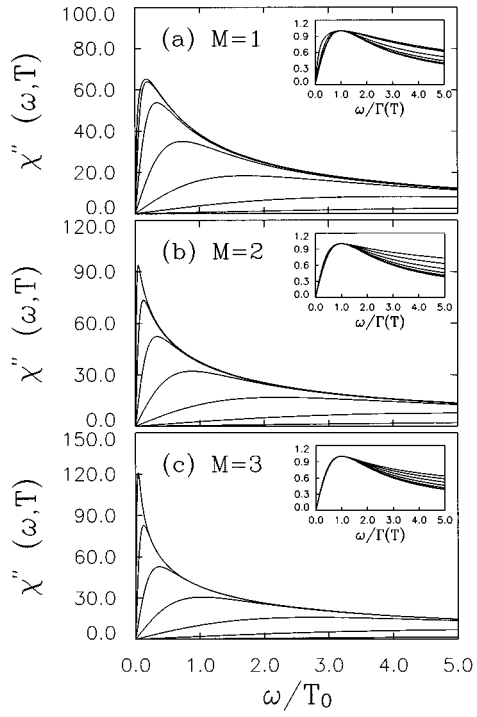

FIG. 14. Variation of $\chi''(\omega)$ with temperature. The dynamic magnetic susceptibility $\chi''(\omega,T)$ is displayed as a function of ω/T_0. The reduced ones $\chi''(\omega,T)/\chi''(\Gamma(T),T)$ are displayed in the insets as a function of $\omega/\Gamma(T)$ and show a rough scaling behavior between two exrema. $\Gamma(T)$ is the peak position of the dynamic magnetic susceptibility. One-channel case, model set 8; two-channel case, model set 1; three-channel case, model set 4. The temperature variations are the same as in Fig. 9 except for an additional low temperature $T=2.321\times10^{-5}$.

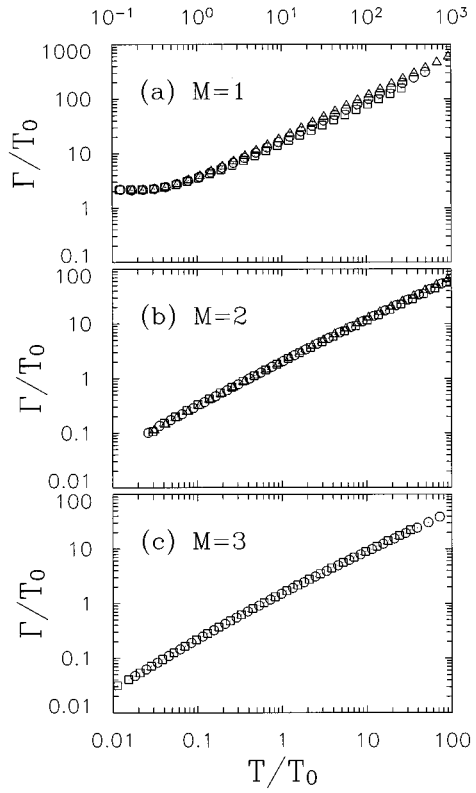

FIG. 15. Peak position $[\Gamma(T)]$ of the dynamic magnetic susceptibility. The temperature variation of $\Gamma(T)$ depends on the relevant channel numbers. In the one-channel case (a), $\Gamma(T)$ approaches a constant value as $T\rightarrow0$. In the two- or three-channel cases (b) and (c), $\Gamma(T\rightarrow0)\rightarrow0$ which is none other than marginal Fermi-liquid behavior. Symbols have the same meaning as in Fig. 6. Note the different temperature ranges between the $M=1$ case (top) and $M=2,3$ cases (bottom).

conduction electrons close to the impurity site will pass through it in a time τ_c of the order of $1/T$ from the uncertainty principle. At high temperatures above the Kondo temperature, $\tau_f\gg\tau_c$. Thus the impurity spin rarely flips while conduction electrons pass by the impurity site. Hence Curie-law behavior is expected in the magnetic susceptibility. At low temperatures, in the one-channel regime, $\tau_f\ll\tau_c$, and the impurity spin flips frequently, so that the average spin moment of the impurity is zero, leading to a Pauli behavior in the susceptibility. In the two- and three-channel regimes, $\tau_f\approx\tau_c$ and spin screening is not complete, leading to the non-Fermi-liquid ground state. This interpretation agrees with the diverging low-temperature behavior of the magnetic susceptibility.

E. Transport coefficients

Using the Kubo formula[6] in a dilute impurity limit, where the interimpurity correlation can be neglected, we have calculated the resistivity and thermopower. The anisotropic conduction electron scattering rate is

$$\tau^{-1}(\hat{k},\omega)=\frac{8\pi n_{\rm imp}}{N(0)}[\Gamma_{01}\Theta_7^{(5/2)}(\hat{k})\rho_{01}(\omega)+\Gamma_{12}\Theta_8^{(5/2)}(\hat{k})\rho_{12}(\omega)], \tag{127}$$

$$\Theta_7^{(5/2)}(\hat{k})=\frac{1}{16\pi}[6-\Phi(\hat{k})],\Theta_8^{(5/2)}(\hat{k})=\frac{1}{16\pi}[6+\Phi(\hat{k})], \tag{128}$$

$$\Phi(\hat{k})=15\cos^4\theta-10\cos^2\theta+1+5\sin^4\theta\cos^2 2\varphi. \tag{129}$$

Here $n_{\rm imp}$ is the impurity concentration.

The transport coefficients are calculated using the Kubo formula under the assumption of dominant scattering in the $l=3$ channel. Our results are defined in terms of transport integrals I_n given by the equations

$$I_n(T)=\int d\omega\omega^n\tau(\omega,T)\left[-\frac{\partial f(\omega)}{\partial\omega}\right], \tag{130}$$

$$\tau(\omega,T)\equiv\int\frac{d\hat{k}}{4\pi}\tau(\hat{k},\omega,T). \tag{131}$$

Here $f(\omega)$ is the Fermi function. In particular, the resistivity is calculated using the equation

$$\frac{1}{\rho(T)}=\frac{ne^2}{m}I_0(T). \tag{132}$$

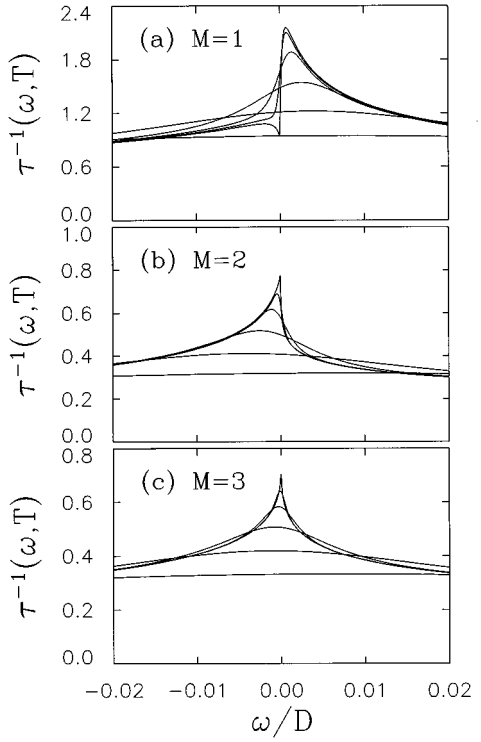

FIG. 16. Angle-averaged scattering rate. (a) One-channel case (model set 8): electron scattering is dominant. The cusp feature for the $M=1$ case right at the Fermi level derives from the spectral depletion of ρ_{12} and zeros of the crystal harmonic $\Theta_7^{(5/2)}(\hat{k})$ which is defined in the text. (b) Two-channel case (model set 1): hole scattering is dominant. (c) Three-channel case (model set 4): weak hole scattering dominance over the electron scattering comes from the degeneracy imbalance between the f^0 singlet and $f^2\Gamma_3$ doublet. The temperature set is the same as in Fig. 9.

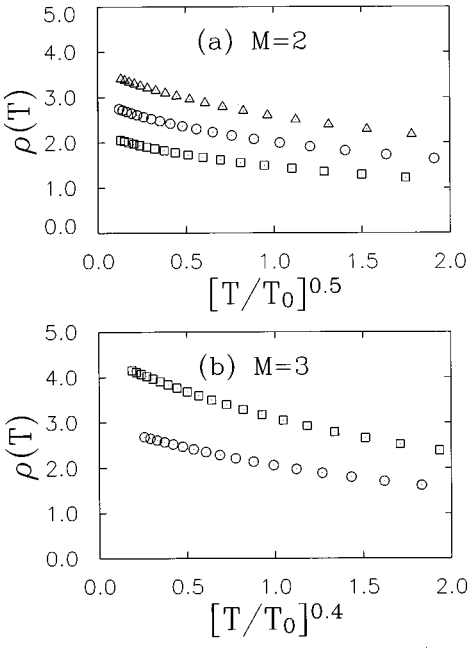

FIG. 17. Low-temperature dependence of resistivity. Correct power laws are found asymptotically for the finite temperature NCA calculation in the two- and three-channel cases. A power law of $T^{1/2}(T^{2/5})$ is expected for $M=2(M=3)$. Symbols have the same meaning as in Fig. 6. The upper bound on the range for the $T^{1/2}(T^{2/5})$ power law is $T_{\max}\approx 0.06T_0(0.18T_0)$ for $M=2(3)$.

Note that the conduction electron scattering rate contains the hybridization since interconfiguration spectral functions are involved. The crystal harmonics are normalized such that the integration of $\int d\hat{k}\Theta_7^{(5/2)}(\hat{k})=1$ and $\int d\hat{k}\Theta_8^{(5/2)}(\hat{k})=2$. Note that the crystal harmonic $\Theta_7^{(5/2)}(\hat{k})$ vanishes at ''hot spot'' angles of $(\theta,\varphi)=(0,-)$, $(\pi,-)$, $(\pi/2,0)$, $(\pi/2,\pi/2)$, $(\pi/2,\pi)$, $(\pi/2,3\pi/2)$, while $\Theta_8^{(5/2)}(\hat{k})$ is positive definite. This feature, combined with the near-Fermi-level ''dip'' in the interconfiguration spectral function for f^1-f^2 excitations $[\rho_{\Gamma_8}(\omega)]$, leads to a reduction in the resistivity at low temperatures in the one-channel parameter regime within our simplified model. We believe that this feature will go away in more realistic models. For example, another contribution to the Γ_8 atomic spectral function comes from the convolution between f^0 and $f^1 J=5/2\Gamma_8$. This spectral function will not be depleted at the Fermi level, but instead will build up its spectral weight due to the weak Kondo resonance structure just above $\omega=0$.

This reduction of the resistivity does not occur in the two- and three-channel regimes. Instead, a Kondo-resonance-related peak develops near the Fermi energy, whose position with respect to the Fermi level depends on whether the model is in the two- or three-channel regime. Details are displayed in Fig. 16. In the two-channel and three-channel model parameter regimes, the resistivity initially increases logarithmically through T_0 and then saturates with a power law to a constant with further decreasing temperatures. The resistivity near zero temperature obeys a scaling behavior as shown in Fig. 17, confirming our zero-temperature analysis with the scaling dimensions $\Delta_2=1/2$, $\Delta_3=2/5$. These results agree with the conformal field theory analysis,[8,9] viz., $\rho(T)=\rho(0)[1-a[T/T_0]^{\Delta_n}]$ for $T\leqslant 0.06T_0$, $\Delta_n=2/(n+2)$ for the overcompensated multichannel Kondo models (note that the power law exponent is independent of the impurity spin size). We note that the region where strict T^{Δ_n} behavior holds is below about $0.05T_0$. A fit to the resistivity of $Ce_xLa_{1-x}Cu_{2.2}Si_2$ (see Fig. 1) is good until low temperatures where the data break below that given by theory. This suggests a possible crossover to a new fixed point which could be set by intersite interactions (producing a spin molecular field) or a weak noncubic symmetry for the Ce^{3+} ions.

The thermopower $Q(T)$ is a sensitive measure of the asymmetry in the scattering rate and the density of states (DOS) near the Fermi level. Since we are assuming a particle-hole-symmetric Lorentzian or Gaussian DOS for the conduction band, the sign of the thermopower is determined by the asymmetry in the scattering rate. Our expression for the thermopower $Q(T)$ is

$$Q(T)=-\frac{1}{eT}\frac{I_1(T)}{I_0(T)}. \tag{133}$$

Our full results for the thermopower are displayed and discussed in Ref. 16 and will not be repeated here. Instead, we just briefly summarize the results below. There we showed that at low temperatures the thermopower is positive in the

one-channel regime, negative in the two-channel regime, and weakly negative in the three-channel regime. The reason is that a strong hybridization between f^0 and f^1 affects the dominant scattering of electrons from the enhanced spectral weight above the Fermi level. Since particle scattering dominates, holes are the main carriers in the one-channel case, and a positive thermopower arises. On the other hand, a negative thermopower arises when the hybridization is strongest in the f^1-f^2 sector. In this case, more spectral weight arises below the Fermi energy, so that holes are scattered more strongly and electrons carry thermal current, leading to a negative thermopower. In the three-channel regime, energy structures are symmetric. However, the double degeneracy in the f^2 configuration leads to weakly dominant hole scattering, resulting in a negative thermopower at low temperatures. The overall magnitude of the thermopower is slightly reduced when anisotropy at the cubic sites is included.

VI. DISCUSSION AND CONCLUSION

We have introduced and studied a realistic model Hamiltonian for Ce^{3+} impurities with three configurations (f^0, f^1, f^2), which are embedded in cubic normal metals. This simple model shows competition between the Fermi-liquid fixed point of the one-channel $S=1/2$ Kondo model and the non-Fermi-liquid fixed point of the two-channel $S=1/2$ Kondo model.

We studied this simplified Anderson model using the NCA. This simple model covers one-, two-, and three-channel Kondo physics depending on the model parameters. All the calculated physical quantities show the signatures of the Kondo effect appropriate to the different numbers of relevant channels. The static magnetic susceptibility agrees with the exact Bethe ansatz and conformal field theory results for the two- and three-channel model parameter regimes. Entropy and specific heat calculations for the two- and three-channel regimes are also in agreement with the Bethe ansatz results, with a discrepancy of the order of a few percent in the estimated residual entropy attributable to $O(1/N^2)$ corrections to the theory (vertex corrections).

Our new results are for transport coefficients and dynamical spectra. Conformal theory is only able to predict the low-temperature and low-frequency behavior of the dynamical spectra and transport coefficients and not the quantitative crossover from high to low temperatures. In the one-channel regime, the model yields a nonmonotonic resistivity which we believe to be spurious. In the two- and three-channel regimes, the resistivity increases logarithmically and saturates as $1-(T/T_0)^{a(M)}$ with decreasing temperatures (where $M=2,3$ is the channel number). The low-temperature behavior power law saturation is in agreement with the conformal field theory results.

Since the thermopower is very sensitive to the density of states structure and the scattering mechanism near the Fermi level, its sign and its magnitude give a measure of the low-temperature fixed point. In the one-channel regime, electrons are strongly scattered due to the Kondo resonance above the Fermi level and the thermopower remains positive definite and large. In the two-channel case, holes are scattered off the impurity sites stronger than electrons. Thus electrons are the main carriers, leading to a negative thermopower. In the three-channel regime, although hole scattering is reduced compared to the two-channel case, electrons are still the main carriers due to the degeneracy imbalance between the singlet f^0 and the doublet $f^2 J=4\Gamma_3$. The thermopower remains negative but very small. We note that our thermopower calculations omit the contributions of excited crystal field levels and so may not compare quantitatively with results on $CeCu_2Si_2$ and its alloys.

We calculated the dynamic magnetic susceptibility and characterized it in terms of the peak position $[\Gamma(T)]$ as a function of temperature. We see a clear difference between the one-channel and overcompensated cases. While $\Gamma(T)$ decreases and saturates to a constant value of order T_K with decreasing temperatures in the one-channel case, $\Gamma(T)$ goes to zero almost linearly with decreasing temperatures in the two- and three-channel cases.

We now discuss the experimental relevance of our model study to the $Ce_{1-x}La_xCu_{2.2}Si_2$ alloy.[17] We have already stressed the experimental evidences supporting the two-channel Kondo effect in this alloy system in Sec. I. The thermopower for $CeCu_2Si_2$ changes sign around 70 K and is negative and large below.[18,49] As our numerical calculation shows, the thermopower is negative and large in the two-channel regime. This result compares well with the experimental findings for the stoichiometric system with $x=1$. We believe the sign change comes from the Kondo resonance of f^0 and $f^1\Gamma_8$, which lies above the Fermi level. Further experiments are required for the alloy system with excess Cu. For comparison, we note that $CeAl_2$ or $CeAl_3$ (Ref. 49) has a positive thermopower large compared to transition metals at high temperatures and has a sign change at low temperature which is still larger than the Kondo temperature. Our thermopower calculation and the thermopower dependence on the unit cell volume[50] suggests that the alloy system $Ce_{1-x}La_xCu_{2.2}Si_2$ can go through the three-channel model parameter regime with external pressure. Renormalized atom calculations further suggest a destabilization of f^2 relative to f^0 with initial increasing pressure.[38] We note that measurements of the $x=0.1$ samples give a low-temperature positive thermopower.[51,52] If the two-channel fixed-point interpretation is correct for this alloy, the only clear way this may be reconciled with our results is through a calculation which properly includes the excited crystal field levels, which in principle can render the thermopower positive.

In addition to the thermopower, neutron scattering experiments for the $Ce_{1-x}La_xCu_{2.2}Si_2$ alloy can search for the unusual temperature dependence of $\Gamma(T)$ (the peak position of the dynamic magnetic susceptibility) to see if it is consistent with our interpretation in terms of the two-channel limit of the model presented herein.

ACKNOWLEDGMENTS

This research was supported by a grant from the U.S. Department of Energy, Office of Basic Energy Sciences, Division of Materials Research. We thank Eunsik Kim for her careful reading of this paper and thank L. N. Oliveira and J.W. Wilkins for stimulating interactions, and F. Steglich for sharing the data of Ref. 51 prior to publication.

APPENDIX A: NCA SELF-ENERGY IN THE PRESENCE OF MULTIPLE IRREPS WITH THE SAME LABEL

In the f^2 configuration, there are nine irreducible representations (irreps) of Γ_3 in a cubic symmetry. All contribute to the effective Schrieffer-Wolff exchange interactions, and the NCA should capture this physics in the leading-order diagrams. Accordingly, the NCA formalism should be appropriately generalized to get the right Kondo energy scale. As an example, we may consider the mixing process between $f^1 J=5/2\Gamma_7$ and $f^2\Gamma_3$. The relevant NCA integral equations are

$$\Sigma(\omega)=\frac{2}{\pi}\sum_{ij}\sqrt{\Gamma_i\Gamma_j}\int d\epsilon f(\epsilon)\tilde{N}(\epsilon)D_{ij}(\epsilon+\omega), \quad \text{(A1)}$$

$$\Pi_{ij}(\omega)=\frac{2}{\pi}\sqrt{\Gamma_i\Gamma_j}\int d\epsilon f(-\epsilon)\tilde{N}(\epsilon)G(\epsilon+\omega). \quad \text{(A2)}$$

Only the conduction electrons of only Γ_8 symmetry are involved in the mixing process. The $f^2\Gamma_3$ Green's function now becomes a 9×9 matrix. This generalization can be seen most clearly by looking at the self-energy diagrams of $f^2\Gamma_3$'s. The incoming Γ_3 does not need to be the same as the outgoing Γ_3. This leads to the matrix Green's function for $f^2\Gamma_3$'s.

According to the Schrieffer-Wolff transformation, the effective Hamiltonian is

$$H_1=J\sum_n \vec{S}_I\cdot\vec{S}_{cn}(0), \quad J=\sum_{i=1}^{9}\frac{2|V_{12}^i|^2}{\epsilon_2^i-\epsilon_1}. \quad \text{(A3)}$$

Now we can show that the above NCA integral equations lead to the right Kondo energy scale to leading order. At this order, no self-energy needs to be inserted into the f^1 propagators, and so we take

$$G(\omega)\rightarrow\frac{1}{\omega-\epsilon_1+i\delta}. \quad \text{(A4)}$$

With this replacement, the Γ_3 self-energy matrix becomes

$$\Pi_{ij}(\omega)=\frac{2}{\pi}\sqrt{\Gamma_i\Gamma_j}\ln\left|\frac{\omega-\epsilon_1}{\omega-D-\epsilon_1}\right| \quad \text{(A5)}$$

for a symmetric flat conduction band DOS with a half width D. Now the Kondo energy scale is determined by

$$\det[(\omega-\epsilon_2^i)\delta_{ij}-\Pi_{ij}(\omega)]=0. \quad \text{(A6)}$$

With the substitution $\omega=\epsilon_1-T_0$, we can find

$$\ln\left|\frac{T_0}{D+T_0}\right|=\frac{1}{N(0)J}, \quad \text{(A7)}$$

$$N(0)J=\frac{2}{\pi}\sum_{i=1}^{9}\frac{\Gamma_i}{\epsilon_2^i-\epsilon_1}. \quad \text{(A8)}$$

Here $\Gamma_i=\pi N(0)|V_{12}^i|^2$.

In conclusion, we have shown that the inclusion of all the Γ_3's in the f^2 configuration leads to an enhanced two-channel exchange coupling.

APPENDIX B: ZERO-TEMPERATURE ANALYSIS: OVERCOMPENSATED MULTICHANNEL ANDERSON MODEL

We discuss the following NCA integral equations at zero temperature.

$$G_g(z)=\frac{1}{z-\epsilon_g-\Sigma_g(z)}, \qquad \Sigma_g(z)=\frac{N_x\Gamma}{\pi}\int d\epsilon\tilde{N}(-\epsilon)f(\epsilon)G_x(z+\epsilon), \quad \text{(B1)}$$

$$G_x(z)=\frac{1}{z-\epsilon_x-\Sigma_x(z)}, \qquad \Sigma_x(z)=\frac{N_g\Gamma}{\pi}\int d\epsilon\tilde{N}(\epsilon)f(\epsilon)G_g(z+\epsilon). \quad \text{(B2)}$$

Here $\tilde{N}(\epsilon)$ is the normalized DOS such that $\tilde{N}(0)=1$. For definiteness, we assume that the excited state has one less electron than the ground state. Before diving into the zero-temperature analysis, we point out the applicability of the NCA approach to the Anderson impurity model. Whenever the ground and excited states have degeneracies of N_g and N_x, respectively, the above form of the NCA integral equations is obtained. The above NCA integral equations also derive from the N_x-channel, $S_I=(N_g-1)/2$ models. This is an artifact of the NCA approach. The NCA cannot distinguish between these two different models. Note that not all Anderson models with degeneracies of N_g (the ground state) and N_x (the excited state) map into the N_x-channel, $S_I=(N_g-1)/2$ models. The Schrieffer-Wolff transformation is essential to see this connection clearly. As an example, the excited triplets in the $f^2 J=4$ in our Ce^{3+} model lead to the one-channel exchange interaction of the impurity $f^1\Gamma_7$ pseudospin $S_I=1/2$ coupled to the $S_c=3/2$ conduction electrons[35] instead of three-channel Kondo model. With this restriction in mind, we now study the zero-temperature analysis of the above NCA integral equations.[14,48]

The dynamical quantities we are interested in are

$$\rho(\omega)=\int d\epsilon[a_x(\epsilon)A_g(\epsilon+\omega)+A_x(\epsilon)a_g(\epsilon+\omega)], \quad \text{(B3)}$$

$$\chi_g''(\omega)=\int d\epsilon[a_g(\epsilon)A_g(\epsilon+\omega)-A_g(\epsilon)a_g(\epsilon+\omega)], \quad \text{(B4)}$$

$$a_g(\omega)\equiv\frac{e^{-\beta\omega}}{Z_f}A_g(\omega), \quad a_x(\omega)\equiv\frac{e^{-\beta\omega}}{Z_f}A_x(\omega). \quad \text{(B5)}$$

We can show that

$$a_g(\omega)|G_g(\omega)|^{-2}=\frac{N_x\Gamma}{\pi}\int d\epsilon\tilde{N}(-\epsilon)f(-\epsilon)a_x(\omega+\epsilon), \quad \text{(B6)}$$

$$a_x(\omega)|G_x(\omega)|^{-2}=\frac{N_g\Gamma}{\pi}\int d\epsilon\tilde{N}(\epsilon)f(-\epsilon)a_g(\omega+\epsilon). \quad \text{(B7)}$$

At zero temperature, the Fermi function is reduced to a step function. Thus, the self-energy equations are simplified to

$$\Sigma_g(z)=\frac{N_x\Gamma}{\pi}\int_{-\infty}^{0}d\epsilon\widetilde{N}(-\epsilon)G_x(z+\epsilon), \tag{B8}$$

$$\Sigma_x(z)=\frac{N_g\Gamma}{\pi}\int_{-\infty}^{0}d\epsilon\widetilde{N}(\epsilon)G_g(z+\epsilon), \tag{B9}$$

$$a_g(\omega)|G_g(\omega)|^{-2}=\frac{N_x\Gamma}{\pi}\int_{0}^{\infty}d\epsilon\widetilde{N}(-\epsilon)a_x(\omega+\epsilon), \tag{B10}$$

$$a_x(\omega)|G_x(\omega)|^{-2}=\frac{N_g\Gamma}{\pi}\int_{0}^{\infty}d\epsilon\widetilde{N}(\epsilon)a_g(\omega+\epsilon). \tag{B11}$$

For a flat conduction band with a cutoff, $[-D,D]$, we can reduce the above equations to the differential equations

$$g_g(\omega)=-1/G_g(\omega),\quad g_x(\omega)=-1/G_x(\omega), \tag{B12}$$

$$\frac{d}{d\omega}g_g(\omega)=-1-\frac{N_x\Gamma}{\pi}\frac{1}{g_x(\omega)},\quad g_g(-D)=D+\epsilon_g, \tag{B13}$$

$$\frac{d}{d\omega}g_x(\omega)=-1-\frac{N_g\Gamma}{\pi}\frac{1}{g_g(\omega)},\quad g_x(-D)=D+\epsilon_x, \tag{B14}$$

$$\frac{d}{d\omega}[a_g(\omega)|g_g(\omega)|^2]=-\frac{N_x\Gamma}{\pi}a_x(\omega), \tag{B15}$$

$$\frac{d}{d\omega}[a_x(\omega)|g_x(\omega)|^2]=-\frac{N_g\Gamma}{\pi}a_g(\omega). \tag{B16}$$

Removing the ω dependence, we find the relationship between g_g and g_x, in terms of the integration constant which connects the low-energy and high-energy states, given through the equation

$$\frac{g_g}{D+\epsilon_g}=\exp\left[\frac{\pi(\epsilon_g-\epsilon_x)}{N_g\Gamma}\right]\exp\left[-\frac{\pi(g_g-g_x)}{N_g\Gamma}\right]\left[\frac{g_x}{D+\epsilon_x}\right]^{N_x/N_g}. \tag{B17}$$

Since the zero-temperature analysis is meaningful only when $D\gg\epsilon_{g,x}$, we will replace $D+\epsilon_{g,x}$ by D. That is,

$$\frac{g_g}{T_0}=\exp\left[-\frac{\pi(g_g-g_x)}{N_g\Gamma}\right]\left[\frac{g_x}{\Delta}\right]^{N_x/N_g}, \tag{B18}$$

$$T_0=D\left[\frac{\Delta}{D}\right]^{N_x/N_g}\exp\left[\frac{\pi(\epsilon_g-\epsilon_x)}{N_g\Gamma}\right], \tag{B19}$$

$$\Delta=\frac{\Gamma}{\pi}, \tag{B20}$$

and

$$\frac{d}{d\omega}[N_g a_g(\omega)g_g(\omega)+N_x a_x(\omega)g_x(\omega)] =N_g a_g(\omega)+N_x a_x(\omega). \tag{B21}$$

Due to the sharpness of the Fermi function at the Fermi level, the spectral functions have a sharp cutoff at the threshold energy E_0. Since $A_n(\omega)$ vanishes below this cutoff energy, $\Sigma_n(\omega)$ is purely real and $g_n(\omega)$ does not vanish or cross the frequency axis below the threshold energy E_0. That is, $g_n(\omega)$ is positive definite below the threshold energy E_0.

1. Leading asymptotic behavior

We can derive the asymptotic behavior near the cutoff energy. Since $a_g(\omega)$ and $g_x(\omega)$ vanish at $\omega=E_0$, we can approximate the above equations:

$$E_0-\omega=\int_0^{g_x}dy\,\frac{g_g(y)}{g_g(y)+N_g\Delta}\approx\frac{1}{N_g\Delta}\int_0^{g_x}dy\,g_g(y), \tag{B22}$$

$$E_0-\omega=\int_0^{g_g}dy\,\frac{g_x(y)}{g_x(y)+N_x\Delta}\approx\frac{1}{N_x\Delta}\int_0^{g_g}dy\,g_x(y), \tag{B23}$$

$$\frac{g_g}{T_0}\approx\left[\frac{g_x}{\Delta}\right]^{N_x/N_g}. \tag{B24}$$

Here $\Delta=\Gamma/\pi$. From the above, we can find

$$\frac{g_g(\omega)}{T_0}\approx|\widetilde{\Omega}|^{\alpha_g}, \tag{B25}$$

$$\frac{g_x(\omega)}{\Delta}\approx|\widetilde{\Omega}|^{\alpha_x}, \tag{B26}$$

$$T_0=D\left[\frac{\Delta}{D}\right]^{N_x/N_g}\exp\left[\frac{\pi(\epsilon_g-\epsilon_x)}{N_g\Gamma}\right], \tag{B27}$$

$$\alpha_g=\frac{N_x}{N_g+N_x},\quad \alpha_x=\frac{N_g}{N_g+N_x}, \tag{B28}$$

$$\widetilde{\Omega}\equiv(N_g+N_x)\frac{E_0-\omega}{T_0}. \tag{B29}$$

Since the zero-temperature analysis is based upon the assumption $|\epsilon_n|\ll D$, the realistic Kondo energy scale is given by the replacement of $D+\epsilon_n\to D$. The asymptotic behavior right above the cutoff E_0 can be found from the expressions below E_0 by the analytic continuation

$$\frac{g_g(\omega+i\delta)}{T_0}\approx e^{-i\alpha_g\pi}\widetilde{\Omega}^{\alpha_g}, \tag{B30}$$

$$\frac{g_x(\omega+i\delta)}{\Delta}\approx e^{-i\alpha_x\pi}\widetilde{\Omega}^{\alpha_x}, \tag{B31}$$

$$A_g(\omega)\approx\frac{1}{\pi T_0}\sin(\alpha_g\pi)|\widetilde{\Omega}|^{-\alpha_g}\theta(\omega-E_0), \tag{B32}$$

$$A_x(\omega)\approx\frac{1}{\pi\Delta}\sin(\alpha_x\pi)|\widetilde{\Omega}|^{-\alpha_x}\theta(\omega-E_0). \tag{B33}$$

Here the phase was determined such that the spectral function is positive definite above the threshold energy. Since $[N_g a_g g_g+N_x a_x g_x]_{\omega=E_0}=1$, we can deduce that

$$a_g(\omega)\approx\frac{1}{(N_g+N_x)T_0}\widetilde{\Omega}^{-\alpha_g}\theta(E_0-\omega), \tag{B34}$$

$$a_x(\omega)\approx\frac{1}{(N_g+N_x)\Delta}\widetilde{\Omega}^{-\alpha_x}\theta(E_0-\omega). \tag{B35}$$

From the above asymptotic expressions, we find

$$\rho(\omega)\approx\frac{1}{\Gamma}\frac{1}{(N_g+N_x)^2}B(\alpha_x,\alpha_g)\times\begin{cases}\sin(\alpha_g\pi)\,\theta(\omega)\\ \sin(\alpha_x\pi)\,\theta(-\omega)\end{cases}$$
$$=\frac{1}{\Delta}\frac{1}{[N_g+N_x]^2}, \tag{B36}$$

$$\chi_g''(\omega)\approx\frac{1}{\pi T_0}\frac{\sin(\alpha_g\pi)}{(N_g+N_x)^2}B(\alpha_x,\alpha_x)\mathrm{sgn}(\omega)|\widetilde{\omega}|^{1-2\alpha_g}, \tag{B37}$$

$$\widetilde{\omega}\equiv(N_g+N_x)\frac{\omega}{T_0}. \tag{B38}$$

Here $B(p,q)$ is the β function.

2. Next leading asymptotic behavior

From the above analysis, we can see that it is more appropriate to use dimensionless quantities. Here we collect all the relevant formulas from the above:

$$\frac{d}{d\widetilde{\Omega}}\frac{g_g}{T_0}=\alpha_g\left[\frac{1}{N_x}+\frac{\Delta}{g_x}\right],\quad g_g(-D)=D+\epsilon_g, \tag{B39}$$

$$\frac{d}{d\widetilde{\Omega}}\frac{g_x}{\Delta}=\alpha_x\left[\frac{T_0}{N_g\Delta}+\frac{T_0}{g_g}\right],\quad g_x(-D)=D+\epsilon_x, \tag{B40}$$

$$\frac{d}{d\widetilde{\Omega}}[a_g(\omega)|g_g(\omega)|^2]=\alpha_g\Delta T_0 a_x(\omega), \tag{B41}$$

$$\frac{d}{d\widetilde{\Omega}}[a_x(\omega)|g_x(\omega)|^2]=\alpha_x\Delta T_0 a_g(\omega), \tag{B42}$$

$$E_0-\omega=\int_0^{g_x}dy\,\frac{g_g(y)}{g_g(y)+N_g\Delta}, \tag{B43}$$

$$E_0-\omega=\int_0^{g_g}dy\,\frac{g_x(y)}{g_x(y)+N_x\Delta}, \tag{B44}$$

$$\frac{g_g}{T_0}=\exp\left[-\frac{\pi(g_g-g_x)}{N_g\Gamma}\right]\left[\frac{g_x}{\Delta}\right]^{N_x/N_g}. \tag{B45}$$

Expanding the last relation, we get

$$\frac{g_g}{T_0}=\left[\frac{g_x}{\Delta}\right]^{N_x/N_g}\left(1+\frac{g_x}{N_g\Delta}-\frac{T_0}{N_g\Delta}\left[\frac{g_x}{\Delta}\right]^{N_x/N_g}+\cdots\right). \tag{B46}$$

Then it is straightforward to show that

$$\frac{g_g}{T_0}=\widetilde{\Omega}^{\alpha_g}[1-g_1\widetilde{\Omega}^{\alpha_g}+2g_2\widetilde{\Omega}^{\alpha_x}+\cdots], \tag{B47}$$

$$\frac{g_x}{\Delta}=\widetilde{\Omega}^{\alpha_x}[1+2g_1\widetilde{\Omega}^{\alpha_g}-g_2\widetilde{\Omega}^{\alpha_x}+\cdots], \tag{B48}$$

$$g_1=\frac{1}{N_g+2N_x}\frac{T_0}{\Delta},\quad g_2=\frac{1}{2N_g+N_x}. \tag{B49}$$

Furthermore, writing in a Taylor expansion form,

$$a_g=\frac{1}{[N_g+N_x]T_0}\widetilde{\Omega}^{-\alpha_g}[1+a_1\widetilde{\Omega}^{\alpha_g}+a_2\widetilde{\Omega}^{\alpha_x}+\cdots]\theta(\widetilde{\Omega}), \tag{B50}$$

$$a_x=\frac{1}{[N_g+N_x]\Delta}\widetilde{\Omega}^{-\alpha_x}[1+b_1\widetilde{\Omega}^{\alpha_g}+b_2\widetilde{\Omega}^{\alpha_x}+\cdots]\theta(\widetilde{\Omega}), \tag{B51}$$

we can find the relations

$$b_1=2a_1-4g_1,\quad \alpha_g b_2=a_2+4g_2, \tag{B52}$$

$$\alpha_x a_1=b_1+4g_1,\quad a_2=2b_2-4g_2. \tag{B53}$$

Finally we find

$$a_g=\frac{1}{[N_g+N_x]T_0}\widetilde{\Omega}^{-\alpha_g}[1+0\widetilde{\Omega}^{\alpha_g}-4g_2\widetilde{\Omega}^{\alpha_x}+\cdots]\theta(\widetilde{\Omega}), \tag{B54}$$

$$a_x=\frac{1}{[N_g+N_x]\Delta}\widetilde{\Omega}^{-\alpha_x}[1-4g_1\widetilde{\Omega}^{\alpha_g}+0\widetilde{\Omega}^{\alpha_x}+\cdots]\theta(\widetilde{\Omega}). \tag{B55}$$

In this limit, the pseudoparticle spectral functions are

$$A_g=\frac{1}{\pi T_0}|\widetilde{\Omega}|^{-\alpha_g}\{\sin(\alpha_g\pi)-2g_2\sin[(\alpha_g-\alpha_x)\pi]|\widetilde{\Omega}|^{\alpha_x}+\cdots\}\theta(-\widetilde{\Omega})$$
$$=\frac{\sin(\alpha_g\pi)}{\pi T_0}|\widetilde{\Omega}|^{-\alpha_g}\{1+4g_2\cos(\alpha_g\pi)|\widetilde{\Omega}|^{\alpha_x}+\cdots\}\theta(-\widetilde{\Omega}), \tag{B56}$$

$$A_x=\frac{\sin(\alpha_g\pi)}{\pi\Delta}|\widetilde{\Omega}|^{-\alpha_x}\{1-4g_1\cos(\alpha_g\pi)|\widetilde{\Omega}|^{\alpha_g}+\cdots\}\theta(-\widetilde{\Omega}). \tag{B57}$$

The scaling dimensions found here all agree with those found in the conformal field theory for the overcompensated cases.

3. Physical quantities

Using the above results, we can find the dynamic susceptibilities for the ground and excited configurations

$$\chi_g''(\omega)=\mathrm{sgn}(\omega)\frac{\sin(\alpha_g\pi)}{(N_g+N_x)^2\pi T_0}\{B(\alpha_x,\alpha_x)|\widetilde{\omega}|^{1-2\alpha_g}$$
$$-4g_2[1-\cos(\alpha_g\pi)]$$
$$\times B(\alpha_x,2\alpha_x)|\widetilde{\omega}|^{2-3\alpha_g}+\cdots\}, \tag{B58}$$

$$\chi_x''(\omega)=\mathrm{sgn}(\omega)\frac{T_0\sin(\alpha_x\pi)}{(N_g+N_x)^2\pi\Delta^2}\{B(\alpha_g,\alpha_g)|\tilde{\omega}|^{1-2\alpha_x} -4g_1[1-\cos(\alpha_x\pi)] \times B(\alpha_g,2\alpha_g)|\tilde{\omega}|^{2-3\alpha_x}+\cdots\}. \quad \text{(B59)}$$

These are the imaginary parts of the corresponding full dynamic susceptibility functions. The functional forms are of marginal Fermi-liquid type for the overcompensated case $N_g=N_x$. The local electron spectral functions are

$$\rho_f(\omega>0)=\frac{\sin(\alpha_g\pi)}{(N_g+N_x)^2\pi\Delta} \times\{B(\alpha_x,\alpha_g)-4g_1B(\alpha_x,2\alpha_g)|\tilde{\omega}|^{\alpha_g} +4g_2\cos(\alpha_g\pi)B(\alpha_g,2\alpha_x)|\tilde{\omega}|^{\alpha_x}+\cdots\}, \quad \text{(B60)}$$

$$\rho_f(\omega<0)=\frac{\sin(\alpha_x\pi)}{(N_g+N_x)^2\pi\Delta} \times\{B(\alpha_x,\alpha_g)+4g_1\cos(\alpha_x\pi)B(\alpha_x,2\alpha_g)|\tilde{\omega}|^{\alpha_g} -4g_2B(\alpha_g,2\alpha_x)|\tilde{\omega}|^{\alpha_x}+\cdots\}. \quad \text{(B61)}$$

One important observation is that the scaling dimensions agree with those obtained from conformal field theory treatments for overcompensated multichannel $S=1/2$ models. From this result, we can argue that the local electron spectral function is peaked right at the Fermi level (Kondo resonance) for overcompensated models. This result seems to be independent of the occupancy of the ground level. In fact, numerical results with the NCA confirm this conclusion. Hence we conclude that the Kondo resonance peak in the overcompensated models sits right at the Fermi level irrespective of any model parameters. In the single-channel Anderson model, the position of the Kondo resonance peak is adjusted by the Friedel sum rule (Fermi-liquid ground state). That is, the occupancy of the ground configuration determines the Kondo resonance peak position.

We can also generate the low-temperature dependence of some physical quantities. Resistivity and thermopower can be evaluated using the Kubo formula.

$$\rho(T)=\rho(0)\left(1-c\left[\frac{T}{T_0}\right]^{\nu}\right), \quad \nu=\min(\alpha_g,\alpha_x), \quad \text{(B62)}$$

$$Q(T)\propto\left[\frac{T}{T_0}\right]^{\nu}. \quad \text{(B63)}$$

APPENDIX C: CONDUCTION ELECTRON SCATTERING RATE

Here we derive the conduction electron scattering time in the presence of Anderson magnetic impurities. In general, the conduction electron scattering rate (the inverse of the conduction electron lifetime) is different from the transport scattering rate. This difference derives from the vertex correction when we calculate the current-current response function. The simplifying feature of the Anderson model is that only one partial wave state is coupled to the atomic electron state for an isotropic hybridization. In this simplified model, the transport scattering rate is proportional to the imaginary part of the conduction electron self-energy.

The conduction electron scattering time is given by the angular average of the anisotropic one:

$$\tau_{\mu\nu}(\omega)=3\int\frac{d\hat{k}}{4\pi}\hat{k}_\mu\hat{k}_\nu\tau_{\mu\nu}(\hat{k},\omega). \quad \text{(C1)}$$

Since $\tau_{\mu\nu}(-\hat{k},\omega)=\tau_{\mu\nu}(\hat{k},\omega)$ in the Anderson model, the scattering time matrix becomes diagonal. Thus we have

$$\tau_{\mu\mu}(\omega)=\int\frac{d\hat{k}}{4\pi}\hat{k}_\mu\hat{k}_\mu\tau(\hat{k},\omega). \quad \text{(C2)}$$

In the dilute Anderson impurity limit, the conduction electron self-energy can be approximated by[6]

$$\Sigma(\vec{k}\alpha,i\omega)=N_{\mathrm{imp}}\sum_i|\langle\vec{k}\alpha|V|i\rangle|^2G_i(i\omega), \quad \text{(C3)}$$

$$\tau^{-1}(\vec{k}\alpha,\omega)=2\pi N_{\mathrm{imp}}\sum_i|\langle\vec{k}\alpha|V|i\rangle|^2\rho_i(\omega). \quad \text{(C4)}$$

Here the index i is the atomic electron's good quantum number. We can write the self-energy as follows.

(1) With LS coupling, but without the CEF,

$$\Sigma(\vec{k}\alpha,i\omega)=N_{\mathrm{imp}}\sum_{jm}|\langle\vec{k}\alpha|V|jm\rangle|^2G_f(j;i\omega), \quad \text{(C5)}$$

$$G_f(j;\tau)=-\langle T_\tau f_{jm}(\tau)f_{jm}^\dagger(0)\rangle, \quad \text{(C6)}$$

$$\langle\vec{k}\alpha|V|jm\rangle=\sum_{m_3\beta}\langle\vec{k}\alpha|V|m_3\beta\rangle\langle 3m_3;\tfrac{1}{2}\beta|jm\rangle. \quad \text{(C7)}$$

The total angular momentum is a good quantum number in this case.

(2) With both LS coupling and the CEF,

$$\Sigma(\vec{k}\alpha,i\omega)=N_{\mathrm{imp}}\sum_{jcd_c}|\langle\vec{k}\alpha|V|\Gamma_c^{(j)}d_c\rangle|^2G_f(\Gamma_c^{(j)};i\omega), \quad \text{(C8)}$$

$$G_f(\Gamma_c^{(j)};\tau)=-\langle T_\tau f_{\Gamma_c^{(j)}d_c}(\tau)f_{\Gamma_c^{(j)}d_c}^\dagger(0)\rangle, \quad \text{(C9)}$$

$$\langle\vec{k}\alpha|V|\Gamma_c^{(j)}d_c\rangle=\sum_m\langle\vec{k}\alpha|V|jm\rangle\langle jm|\Gamma_c^{(j)}d_c\rangle. \quad \text{(C10)}$$

The CEF irreps are good quantum numbers.

In the above, two successive unitary transformations have been used, specified by

$$f_{m_3\alpha}=\sum_{jm}\langle 3m_3;\tfrac{1}{2}\alpha|jm\rangle f_{jm}, \quad \text{(C11)}$$

$$f_{jm}=\sum_{cd_c}\langle jm|\Gamma_c^{(j)}d_c\rangle f_{\Gamma_c^{(j)}d_c}. \quad \text{(C12)}$$

For isotropic, spin-independent hybridization and a free electron conduction band, the mixing matrix is given by

$$\langle \vec{k}\alpha|V|m_3\beta\rangle = \sqrt{\frac{4\pi}{\Omega}} V(k) Y_{3m_3}(\hat{k})\,\delta_{\alpha\beta}, \tag{C13}$$

$$V(k) = \sqrt{4\pi}(-i)^3 \int dr\; r^2 j_3(kr) V(r) R_f(r), \tag{C14}$$

$$\langle \vec{k}\alpha|V|jm\rangle = \sqrt{\frac{4\pi}{\Omega}} V(k) \langle \hat{k}\alpha|jm\rangle, \tag{C15}$$

$$\langle \hat{k}\alpha|jm\rangle = \sum_{m_3} Y_{3m_3}(\hat{k}) \langle 3m_3;\tfrac{1}{2}\,\alpha|jm\rangle, \tag{C16}$$

$$\langle \vec{k}\alpha|V|\Gamma_c^{(j)} d_c\rangle = \sqrt{\frac{4\pi}{\Omega}} V(k) \langle \hat{k}\alpha|\Gamma_c^{(j)} d_c\rangle, \tag{C17}$$

$$\langle \hat{k}\alpha|\Gamma_c^{(j)} d_c\rangle = \sum_{m_3 m} Y_{3m_3}(\hat{k}) \langle 3m_3;\tfrac{1}{2}\,\alpha|jm\rangle \langle jm|\Gamma_c^{(j)} d_c\rangle. \tag{C18}$$

Here Ω is the volume of the system and $R_f(r)$ is the radial part of atomic wave function. Hence the conduction electron self-energy in the isotropic hybridization can be written as

$$\Sigma(\vec{k}\alpha, i\omega) = 4\pi n_{\rm imp} |V(k)|^2 \sum_{jm} |\langle \hat{k}\alpha|jm\rangle|^2 G_f(j; i\omega) \tag{C19}$$

$$= 4\pi n_{\rm imp} |V(k)|^2 \sum_{j c d_c} |\langle \hat{k}\alpha|\Gamma_c^{(j)} d_c\rangle|^2 G_f(\Gamma_c^{(j)}; i\omega). \tag{C20}$$

Here only the diagonal elements of the Green's function are nonvanishing.

1. Without the CEF

When the CEF is neglected, the conduction electron self-energy in a dilute impurity limit reads

$$\Sigma(\vec{k}\alpha, i\omega) = 4\pi n_{\rm imp} |V(k)|^2 \sum_{j} \Theta^{(j)}(\hat{k}) G_f(j; i\omega), \tag{C21}$$

$$\tau^{-1}(\vec{k}\alpha, \omega) = 8\pi^2 n_{\rm imp} |V(k)|^2 \sum_{j} \Theta^{(j)}(\hat{k}) \rho_f(j; \omega), \tag{C22}$$

$$\Theta^{(j)}(\hat{k}) \equiv \sum_{m} |\langle \hat{k}\alpha|jm\rangle|^2. \tag{C23}$$

$\rho_f(j;\omega)$ is the measurable spectral function for the atomic electrons with the total angular momentum j.

The relevant angular functions defined above are, in fact, constants:

$$\Theta^{(j)}(\hat{k}) = \sum_{m} |\langle \hat{k}\alpha|jm\rangle|^2 = \sum_{\mu d_\mu} |\langle \hat{k}\alpha|\Gamma_\mu^{(j)} d_\mu\rangle|^2 = \frac{2j+1}{8\pi}. \tag{C24}$$

2. With the CEF

In the presence of the CEF, the CEF irreducible representations are good quantum numbers. The atomic f-electron operator can be decomposed into CEF irreducible representation components. Hence the conduction electron self-energy in the dilute impurity limit is

$$\Sigma(\vec{k}\alpha, i\omega) = 4\pi n_{\rm imp} |V(k)|^2 \sum_{jc} \Theta_c^{(j)}(\hat{k}) G_f(\Gamma_c^{(j)}; i\omega), \tag{C25}$$

$$\Theta_{\Gamma_c}^{(j)}(\hat{k}) \equiv \sum_{d_c} |\langle \hat{k}\alpha|\Gamma_c^{(j)} d_c\rangle|^2. \tag{C26}$$

Here $\Theta_{\Gamma_c}^{(j)}(\hat{k})$ are crystal harmonics. The anisotropic relaxation rate is

$$\tau^{-1}(\vec{k}\alpha, \omega) = 8\pi^2 n_{\rm imp} |V(k)|^2 \sum_{jc} \Theta_{\Gamma_c}^{(j)}(\hat{k}) \rho_f(\Gamma_c^{(j)}; \omega). \tag{C27}$$

Here $\rho_f(\Gamma_c^{(j)};\omega)$ is the measurable spectral function for the atomic f electron of $\Gamma_c^{(j)}$ symmetry. This spectral function is given by the convolution of two neighboring configuration Green's functions.

In the cubic crystal symmetry, the relevant crystal harmonics are

$$\Theta_7^{(5/2)}(\hat{k}) = \sum_{\alpha} |\langle \hat{k}\uparrow/\downarrow|\Gamma_7^{(5/2)}\alpha\rangle|^2$$
$$= -\frac{1}{32\pi}[35\cos^4\theta - 30\cos^2\theta - 5 + 5\sin^4\theta\cos 4\varphi], \tag{C28}$$

$$\Theta_8^{(5/2)}(\hat{k}) = \sum_{n\alpha} |\langle \hat{k}\uparrow/\downarrow|\Gamma_8^{(5/2)}; n\alpha\rangle|^2$$
$$= \frac{1}{32\pi}[35\cos^4\theta - 30\cos^2\theta + 19 + 5\sin^4\theta\cos 4\varphi], \tag{C29}$$

and

$$\Theta_6^{(7/2)}(\hat{k}) = \sum_{\alpha} |\langle \hat{k}\uparrow/\downarrow|\Gamma_6^{(7/2)};\alpha\rangle|^2$$
$$= \frac{7}{256\pi}[50\cos^6\theta - 30\cos^4\theta - 10\cos^2\theta + \tfrac{34}{3} - 10\sin^4\theta(5\cos^2\theta - 1)\cos 4\varphi], \tag{C30}$$

$$\Theta_7^{(7/2)}(\hat{k}) = \sum_{\alpha} |\langle \hat{k}\uparrow/\downarrow|\Gamma_7^{(7/2)};\alpha\rangle|^2$$
$$= \frac{15}{256\pi}\sin^2\theta[-14\cos^4\theta + 28\cos^2\theta + 2 - 2\sin^2\theta(7\cos^2\theta + 1)\cos 4\varphi], \tag{C31}$$

$$\Theta_8^{(7/2)}(\hat{k}) = \sum_{n\alpha} |\langle \hat{k}\uparrow/\downarrow | \Gamma_8^{(7/2)}; n\alpha\rangle|^2$$

$$= \frac{1}{32\pi}[-70\cos^6\theta + 105\cos^4\theta - 40\cos^2\theta + \tfrac{55}{3} + 5\sin^4\theta(14\cos^2\theta - 1)\cos 4\varphi]. \quad \text{(C32)}$$

Note that the above crystal harmonics are normalized and satisfy the sum rules

$$\int d\hat{k}\Theta_{6,7}^{(j)}(\hat{k}) = 1, \quad \int d\hat{k}\Theta_8^{(j)}(\hat{k}) = 2, \quad \text{(C33)}$$

$$\sum_\mu \Theta_\mu^{(j)}(\hat{k}) = \frac{2j+1}{8\pi}. \quad \text{(C34)}$$

Furthermore, the crystal harmonics for a $j = 5/2$ multiplet can be rewritten as

$$\Theta_7^{(5/2)}(\hat{k}) = \frac{1}{16\pi}[6 - \Phi(\hat{k})], \quad \Theta_8^{(5/2)}(\hat{k}) = \frac{1}{16\pi}[6 + \Phi(\hat{k})], \quad \text{(C35)}$$

$$\Phi(\hat{k}) = 15\cos^4\theta - 10\cos^2\theta + 1 + 5\sin^4\theta\cos^2 2\varphi. \quad \text{(C36)}$$

[1] J. Kondo, Prog. Theor. Phys. **32**, 37 (1964).

[2] P. W. Anderson, Phys. Rev. **124**, 41 (1961).

[3] K. G. Wilson, Rev. Mod. Phys. **47**, 773 (1975); H. R. Krishnamurthy, J. W. Wilkins, and K. G. Wilson, Phys. Rev. B **21**, 1003 (1980); **21**, 1044 (1980).

[4] N. Andrei, K. Furuya, and J. H. Lowenstein, Rev. Mod. Phys. **55**, 331 (1983); A. M. Tsvelick and P. B. Wiegmann, Adv. Phys. **32**, 453 (1983).

[5] H. Keiter and J. C. Kimball, Int. J. Magn. **1**, 233 (1971).

[6] N. E. Bickers, Rev. Mod. Phys. **59**, 845 (1987); N. E. Bickers, D. L. Cox, and J. W. Wilkins, Phys. Rev. B **36**, 2036 (1987).

[7] J. E. Hirsch and R. M. Fye, Phys. Rev. Lett. **56**, 2521 (1986); R. N. Silver, J. E. Gubernatis, D. S. Sivia, and M. Jarrell, *ibid.* **65**, 496 (1990).

[8] I. Affleck and A. W. W. Ludwig, Phys. Rev. Lett. **67**, 161 (1991); A. W. W. Ludwig and I. Affleck, *ibid.* **67**, 3160 (1991); I. Affleck and A. W. W. Ludwig, Phys. Rev. B **48**, 7297 (1993).

[9] A. W. W. Ludwig, Physica B **199&200**, 406 (1994).

[10] P. Nozières and A. Blandin, J. Phys. (Paris) **41**, 193 (1980).

[11] N. Andrei and C. Destri, Phys. Rev. Lett. **52**, 364 (1984).

[12] A. M. Tsvelick and P. B. Wiegmann, Z. Phys. **54**, 201 (1984); A. M. Tsvelick, J. Phys. C **18**, 159 (1985); A. M. Tsvelick and P. B. Wiegmann, J. Stat. Phys. **38**, 125 (1985).

[13] P. D. Sacramento and P. Schlottmann, Phys. Lett. A **142**, 245 (1989); P. D. Sacramento and P. Schlottmann, Phys. Rev. B **43**, 13 294 (1991); P. Schlottmann and P. D. Sacramento, Adv. Phys. **42**, 641 (1993).

[14] D. L. Cox and A. E. Ruckenstein, Phys. Rev. Lett. **71**, 1613 (1993).

[15] P. Nozières, J. Low Temp. Phys. **17**, 31 (1974).

[16] Tae-Suk Kim and D. L. Cox, Phys. Rev. Lett. **75**, 1622 (1995).

[17] B. Andraka, Phys. Rev. B **49**, 3589 (1994).

[18] N. Grewe and F. Steglich, in *Handbook on the Physics and Chemistry of the Rare Earths*, edited by K. A. Gschneidner, Jr. and L. L. Eyring (Elsevier, Amsterdam, 1991), Vol. 14, p. 343; see Fig. 26 [$S(T)$] and Fig. 62 [$\chi(T)$].

[19] E. A. Gorymychin and R. Osborne, Phys. Rev. B **47**, 14 280 (1994), for $CeCu_2Si_2$.

[20] F. G. Aliev, N. B. Brandt, V. V. Moschalkov, and S. M. Chudinov, J. Low Temp. Phys. **57**, 61 (1984); F. Steglich (private communication).

[21] D. L. Cox, Phys. Rev. Lett. **59**, 1240 (1987); Physica C **153-155**, 1642 (1988); J. Magn. Magn. Mater. **76&77**, 53 (1988).

[22] A. Zawadowski, Phys. Rev. Lett. **45**, 211 (1980); A. Muramatsu and F. Guinea, *ibid.* **57**, 2337 (1986).

[23] C. L. Seaman, M. B. Maple, B. W. Lee, S. Ghamaty, M. S. Torikachvili, J.-S. Kang, L. Z. Liu, J. W. Allen, and D. L. Cox, Phys. Rev. Lett. **67**, 2882 (1991); B. Andraka and A. M. Tsvelick, *ibid.* **67**, 2886 (1991).

[24] H. Amitsuka, T. Hidano, T. Honma, H. Mitamura, and T. Sakakibara, Physica B **186-188**, 337 (1993).

[25] B. Andraka and G. R. Stewart, Phys. Rev. B **47**, 3208 (1993).

[26] W. W. Kim, J. S. Kim, B. Andraka, and G. R. Stewart, Phys. Rev. B **47**, 12 403 (1993).

[27] D. A. Gajewski, P. Allenspach, C. L. Seaman, and M. B. Maple, Physica B (to be published).

[28] F. G. Aliev, S. Vieira, R. Villar, H. P. van der Meulen, K. Bakker, and A. V. Andreev, Pis'ma Zh. Éksp. Teor. Fiz. **58**, 814 (1993) [Sov. Phys. JETP Lett. **58**, 762 (1993)]; F. G. Aliev, H. El Mfarrej, S. Vieira, and R. Villar, Solid State Commun. **91**, 775 (1994).

[29] M. B. Maple, C. L. Seaman, D. A. Gajewski, Y. Dalichaouch, V. B. Barbetta, M. C. de Andrada, H. A. Mook, H. G. Lukefahr, O. O. Bernal, and D. E. MacLaughlin, J. Low Temp. Phys. **95**, 225 (1994).

[30] D. C. Ralph and R. Buhrman, Phys. Rev. Lett. **69**, 2118 (1992); D. C. Ralph, A. W. W. Ludwig, Jan von Delft, and R. A. Buhrman, *ibid.* **72**, 1064 (1994); D. C. Ralph and R. Buhrman, Phys. Rev. B **51**, 3554 (1995).

[31] M. Hettler, J. Kroha, and S. Hershfield, Phys. Rev. Lett. **73**, 1967 (1994).

[32] For $Ce_{1-x}La_xCu_6$, see Y. Onuki and T. Komatsubara, J. Magn. Magn. Mater. **63&64**, 281 (1987); for $Ce_{1-x}La_xPb_3$, see C. L. Lin, Phys. Rev. Lett. **58**, 1232 (1987).

[33] A. O. Gogolin, Phys. Rev. B **53**, R5990 (1996).

[34] H. B. Pang and D. L. Cox, Phys. Rev. B **44**, 9454 (1991); I. Affleck, A. W. W. Ludwig, H. B. Pang, and D. L. Cox, *ibid.* **45**, 7918 (1992).

[35] Tae-Suk Kim and D. L. Cox, Phys. Rev. B **54**, 6494 (1996); Tae-Suk Kim, L. N. Oliveira, and D. L. Cox, Phys. Rev. B **55**, 12460 (1997).

[36] M. Kota and H. Shiba, J. Phys. Soc. Jpn. **64**, 4345 (1995).

[37] D. L. Cox, Physica B **186-188**, 312 (1993).

[38] J. F. Herbst and J. W. Wilkins, in *Handbook on the Chemistry and Physics of the Rare Earths*, edited by K. A. Gschneidner and L. Eyring (Elsevier, Amsterdam, 1987), Vol. 10, p. 321.

[39] T.-S. Kim, Ph.D. thesis, The Ohio State University, 1995.

[40] See, for example, M. Tinkham, *Group Theory and Quantum Me-*

chanics (McGraw-Hill, New York, 1964).
[41] J. R. Schrieffer and P. A. Wolff, Phys. Rev. **149**, 491 (1966).
[42] P. W. Anderson, J. Phys. C **3**, 2436 (1970); J. Solyom and A. Zawadowski, J. Phys. F **4**, 2269 (1974).
[43] N. Grewe, Z. Phys. B **52**, 193 (1982).
[44] Y. Kuramoto, Z. Phys. B **53**, 37 (1983).
[45] P. Coleman, Phys. Rev. B **29**, 3035 (1984).
[46] F. C. Zhang and T. K. Lee, Phys. Rev. B **30**, 1556 (1984).
[47] Th. Pruschke and N. Grewe, Z. Phys. B **74**, 439 (1989); Th. Pruschke, Physica B **163**, 553 (1990).
[48] E. Müller-Hartmann, Z. Phys. B **57**, 281 (1984).
[49] D. Jaccard and J. Sierro, in *Valence Instabilities*, edited by P. Watcher and H. Boppart (North-Holland, Amsterdam, 1982), p. 409.
[50] D. Jaccard, K. Behnia, and J. Sierro, Phys. Lett. A **163**, 475 (1992).
[51] B. Buschinger, C. Geibel, and F. Steglich (unpublished).
[52] F. G. Aliev *et al.*, Sov. Phys. Solid State **26**, 682 (1984).